

Observation of chaotic dynamics of coupled nonlinear oscillators

Robert Van Buskirk* and Carson Jeffries

*Department of Physics, University of California, Berkeley, California 94720
and Materials and Molecular Research Division, Lawrence Berkeley Laboratory, Berkeley, California 94720*
(Received 26 September 1984)

The nonlinear charge storage property of driven Si p - n junction passive resonators gives rise to chaotic dynamics: period doubling, chaos, periodic windows, and an extended period-adding sequence corresponding to entrainment of the resonator by successive subharmonics of the driving frequency. The physical system is described; equations of motion and iterative maps are reviewed. Computed behavior is compared to data, with reasonable agreement for Poincaré sections, bifurcation diagrams, and phase diagrams in parameter space (drive voltage, drive frequency). $N=2$ symmetrically coupled resonators are found to display period doubling, Hopf bifurcations, entrainment horns ("Arnol'd tongues"), breakup of the torus, and chaos. This behavior is in reasonable agreement with theoretical models based on the characteristics of single-junction resonators. The breakup of the torus is studied in detail, by Poincaré sections and by power spectra. Also studied are oscillations of the torus and cyclic crises. A phase diagram of the coupled resonators can be understood from the model. Poincaré sections show self-similarity and fractal structure, with measured values of fractal dimension $d=2.03$ and $d=2.23$ for $N=1$ and $N=2$ resonators, respectively. Two line-coupled resonators display first a Hopf bifurcation as the drive parameter is increased, in agreement with the model. For $N=4$ and $N=12$ line-coupled resonators complex quasiperiodic behavior is observed with up to 3 and 4 incommensurate frequencies, respectively.

I. INTRODUCTION

Many physical systems can be viewed as a collection of coupled oscillators or modes. In this paper we report the behavior of N driven nonlinear oscillators, coupled in several ways, for $N=1,2,4,12$. The oscillator is a passive resonator comprised of a silicon p - n junction used as a nonlinear charge-storage element, together with an external inductance. This physical system can be approximately modeled as a driven damped oscillator with a very nonlinear asymmetric restoring force, and has been used previously, first by Linsay¹ who found that it exhibited a period-doubling sequence with convergence ratio δ and power spectra as predicted by Feigenbaum.² It was shown to display other universal behavior patterns³ and has been much studied;⁴ in particular, intermittency,⁵ effects of added noise,^{6,7} and crises^{8,9} have been reported. For two or more coupled resonators (which we also refer to as "oscillators") the system displays a much richer dynamical structure:^{10,11} period doubling, Hopf bifurcations to quasiperiodicity, entrainment horns, and breakup of the invariant torus. This is the main subject of this paper. We view the junction oscillator as an interesting *physical system* from the viewpoint of contemporary nonlinear dynamics theory.¹² It is not an analog computer and is to be clearly distinguished from the numerical solutions of mathematical models that approximately represent it.

To understand coupled junction oscillators we first attempt to understand a single-junction oscillator in detail, in Sec. II: we review the relevant physics of the system and differential equations that, *a priori*, might approximate its behavior. The observed basic oscillator response

function is discussed as well as elementary maps and differential equation models. In Sec. III we show the detailed behavior of a single oscillator by real-time signals, bifurcation diagrams, return maps, phase portraits, Poincaré sections, fractal dimension measurements, and phase diagrams in parameter space. These data are compared to predictions from theoretical models. In Sec. IV we give models for $N=2$ coupled oscillators, present our experimental results, and compare to theory. Section V gives some results for $N=4$ and $N=12$, where quasiperiodicity with up to four frequencies is observed.

II. PHYSICAL SYSTEM AND MODELS

The system. In Fig. 1, the basic nonlinear element is the p - n junction:¹³ a single crystal of Si containing fixed donor ions and electrons to the right and acceptors and holes to the left of an interface in a region $\sim 10^{-4}$ cm wide. One solves the transport equation including drift and mobility terms in an electric field arising from an applied potential difference V . The establishment of electron-hole diffusive equilibrium at the interface results in a built-in potential difference Φ , and parallel layers of fixed donor and acceptor ions, yielding an effective junction differential capacitance $C_j(V)=C_{j0}(1-V/\Phi)^{-1/2}$ for negative applied voltage. If V is positive, forward injection of holes (electrons) into the n (p) regions creates a much larger stored charge limited, however, by the recombination and back diffusion of electrons and holes in minority carrier lifetime τ . For times $t \leq \tau$ the system is approximated by an effective storage differential capacitance $C_s(V)=C_{s0}\exp(V/\phi)$, with $\phi \equiv kT/e$. Figure 2 shows typical data for the total differential capacitance

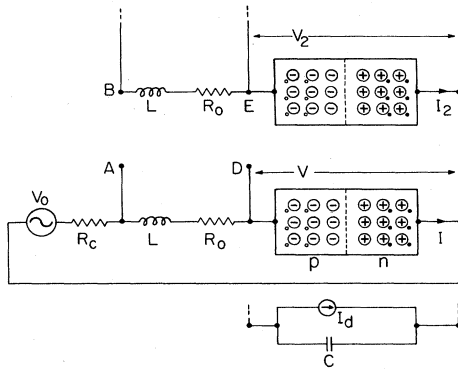


FIG. 1. Experimental system, showing a p - n junction in a Si crystal with fixed donor ions (+) and electrons (\cdot) in the n region, and acceptors ($-$) and holes (\circ) in the p region. A single p - n junction is driven by a sinusoidal voltage $V_0(t)$ through an inductor L and resistances R_C, R_0 . Connecting A to B makes two resistively coupled resonators. Connecting D to B makes two line-coupled resonators. This can be extended to N coupled resonators by connecting E to the next inductor, etc. A junction is modeled by a nonlinear capacitance $C(V)$ in shunt with an ideal Shockley diode $I_d(V)$.

$C(V) = dq/dV = C_j + C_s$ versus V for junctions used here. The junction is modeled by $C(V)$ shunted by an ideal Shockley diode $I_d(V) = I_0[\exp(V/\phi) - 1]$, and is usually driven resonantly through an inductance L by a driving voltage $V_0 = V_{os}\sin(\omega t)$ with $\omega \approx \omega_{res} = [LC(V=0)]^{-1/2}$.

Equations of motion. For a single junction and dynamical variables (I, V, θ) , Kirchoff's laws for Fig. 1 yield three coupled first-order autonomous differential equations:

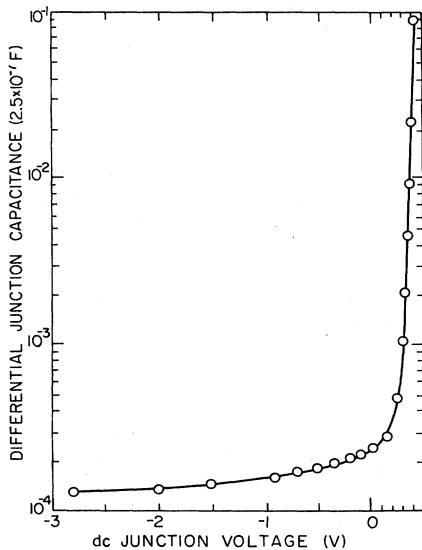


FIG. 2. Measured total differential capacitance $C(V)$ for p - n junction vs junction voltage V . The steep rise is due to charge-storage capacitance $C_s(V)$, the negative voltage region to junction capacitance $C_j(V)$.

$$\dot{I} = \frac{V_0(\theta) - RI - V}{L}, \quad (1a)$$

$$\dot{V} = \frac{I - I_d(V)}{C(V)}, \quad (1b)$$

$$\dot{\theta} = \omega, \quad (1c)$$

where $R = R_C + R_0$ (Fig. 1), and $\theta = \omega t$. The motion can be presented in (I, V, θ) polar coordinates, so chosen that the orbits traverse the (I, V) plane at, say, $\theta = 0, 2\pi, \dots$ at consecutive times determined by the period $T = 2\pi/\omega$ of the driving voltage. This Poincaré section of the attractor can be observed directly by displaying (I, V) on an oscilloscope and strobing the beam intensity at $t = nT$, $n = 1, 2, \dots$. Alternatively, one displays (\dot{I}, I) or (I_{n+1}, I_n) , which are conjectured to be topologically equivalent.¹⁴ Equations (1) are stiff, display a slow and a fast manifold, but can be numerically integrated by an explicit fourth-order Runge-Kutta algorithm.¹⁵

Equations (1) have a form discussed by Ott,¹²

$$dx_i(t)/dt = f_i(x_1(t), x_2(t), x_3(t)), \quad i = 1, 2, 3 \quad (2)$$

and a negative divergence of phase-space flow, $\sum_i \partial f_i / \partial x_i$. For the simpler Eq. (3) the divergence has the value $-|a|$. Phase-space volumes decrease roughly exponentially in time: $\Lambda(t) = \Lambda(0)\exp(-at)$. Since the system is observed to display chaotic motion, one can conclude that it has a strange attractor, characterized by a fractal dimension.

Physical insight comes from calculating the effective junction charge, $q(V) = \int_0^V C(V)dV = \phi C_{s0}[\exp(V/\phi) - 1] + 2\Phi C_{j0}(1 - \sqrt{1 - V/\Phi})$, and rewriting Eqs. (1) in the form of a driven damped oscillator

$$\ddot{q} + a(q)\dot{q} - f(q) = A_0\sin(\omega t), \quad (3)$$

with nonlinear damping coefficient

$$a(q) = \frac{R}{L} + \frac{1}{C(q)} \frac{\partial I_d}{\partial V} \quad (4a)$$

and nonlinear restoring force

$$f(q) = -\frac{1}{L}[V(q) + RI_d(V(q))]. \quad (4b)$$

Figure 3 is a plot of the force function for typical parameter values used and shows a weak, almost constant negative force $f(q) \propto -\ln(q+1)$ for positive q (forward injection). For negative q there is a strong positive force, $f(q) \sim q^2$. For q small, the expansion of Eq. (4b), $f(q) = -Aq + Bq^2 - Cq^3 + Dq^4 + \dots$, shows no symmetry; the system may show period doubling without first a symmetry-breaking bifurcation,¹⁶ in contrast to the driven pendulum and to Duffing's equation with $f(q) \sim -q \pm q^3$. The junction oscillator is so nonlinear it can be driven hard enough to shift its resonant frequency ω_{res} down by an order of magnitude—an ultrasoft spring.

Oscillator response. Figure 4 shows data for the response voltage V of a p - n junction oscillator as a function of frequency, for various values of the driving voltage amplitude. We note the following. (i) A shift down of ω_{res} with increasing V_{os} : a soft spring. (ii) Hysteresis:

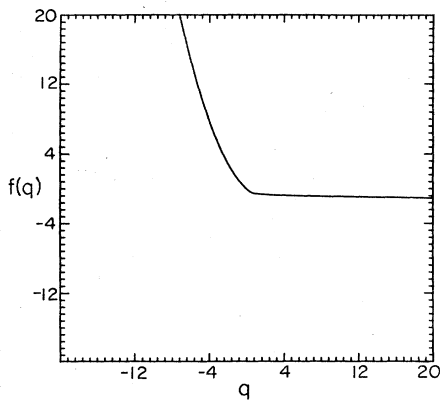


FIG. 3. Nonlinear restoring force $f(q)$ vs q computed from Eq. (4b) using the values $C_{s0}=6 \times 10^{-13}$ F, $C_{j0}=6 \times 10^{-10}$ F, $I_0=4.8 \times 10^{-9}$ A, $\phi=0.04$ V, $\Phi=0.6$ V, $R=90$ Ω , $\omega=4.08 \times 10^5$ sec $^{-1}$, $L=0.01$ H. The units of f and q have been rescaled. Note that $f(0)=0$.

this is the well-known “jump” phenomena for driven nonlinear oscillators;¹⁷ it is a transcritical bifurcation.¹⁸ (iii) Subharmonic response at ω_{res}/n , $n=2,3,4, \dots$, also expected.¹⁷ (iv) Increased resonance width due to increased value of damping coefficient $a(q)$ in Eq. (4a): the junction conducts when driven harder; $a(q)$ switches from R/L at $V < 0.3$ V to $I_0/\phi C_{s0}$ at $V > 0.3$ V, corresponding to a quality factor jump from 120 to ≈ 1 as the junction becomes conducting.

Models. Equations (1) or (3) may be numerically integrated and bifurcation diagrams, Poincaré sections, and

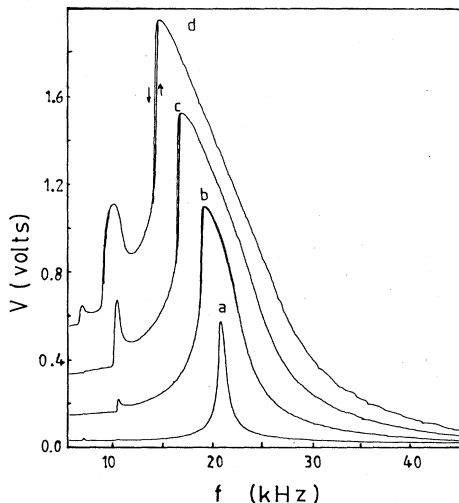


FIG. 4. Junction voltage V vs drive frequency f for a junction resonator for drive voltage V_{os} in mV rms: a, 3; b, 41; c, 103; d, 179. The system is not yet chaotic and responds like a soft spring oscillator with subharmonic response; it also displays jump phenomena, with hysteresis. Type-1N4723 junction, $L=100$ mH, $R=53$ Ω .

return maps computed; this is done below for some cases. The return map may be generally described by a two-dimensional map of the form

$$x_{n+1}=g(x_n, y_n, \Omega), \quad y_{n+1}=h(x_n, y_n, \Omega), \quad (5)$$

where Ω is the set of experimentally adjustable parameters; typically, $\Omega(R, V_{os}, \omega)$. If the system is sufficiently dissipative, the map may reduce to one dimensional, e.g.,

$$x_{n+1}=1-Cx_n^2, \quad (6)$$

the logistic map with one parameter C . In higher order it may reduce to the two-dimensional invertible map of Hénon,

$$x_{n+1}=1-Cx_n^2-y_n, \quad y_{n+1}=Jx_n \quad (7)$$

with an additional parameter J , the Jacobian determinant corresponding to the fractional area contraction per iteration, and thus to the system dissipation; furthermore, with $J \neq 0$ there is hysteresis. As discussed in Sec. III, the driven junction oscillator is only very roughly modeled by Eq. (6) and somewhat better by Eq. (7). It turns out that the behavior can be better modeled by a generalization of Eq. (7),

$$x_{n+1}=f(x_n, \Omega)-y_n, \quad y_{n+1}=Jx_n, \quad (8)$$

where the form of the function f is not simply parabolic but is a unimodal or bimodal function chosen to model the junction oscillator characteristic behavior, e.g., Eq. (10).¹⁰

From the physical fact that the minority carrier density recovery after forward injection is a diffusion process, the motion may be more properly described by differential delay equations rather than Eqs. (1) and (3). *In principle* the system is rather high dimensional, and Eqs. (5) should be generalized to the form $x_{n+1}=g(x_n, x_{n-1}, x_{n-2}, \dots, y_n, y_{n-1}, \dots, \Omega)$, although present data do not seem to require this, owing to the dissipation. The question can be rephrased: how many previous cycles can the system remember in the steady state, i.e., what is the dimension of the phase space?

Simple ODE model. Returning to Eqs. (3) and (4) we make the simplifying assumptions $a(q) \rightarrow \text{const}$; $\omega \rightarrow 1$, driving at resonance; $-f(q) \rightarrow -1 + \exp q$, an exponential force function, to get a simple ordinary differential equation (ODE) model,

$$\ddot{x} + a\dot{x} + e^x - 1 = A \sin t \quad (9)$$

which we numerically integrate to get a rough idea of expected chaotic behavior of driven junctions. Figure 5(a) shows a sequence of computed Poincaré sections, x versus \dot{x} , for consecutive times $t=2\pi(n+\Delta/5)$ for $n=0,1,2, \dots$, and strobe phase $\Delta=0,1,2,3,4,5, \dots$. This shows that under the action of the Poincaré map the attractor, initially at $\Delta=0$, is stretched upward ($\Delta=1,2$), then stretched to the left ($\Delta=3$), then folded down ($\Delta=4$) to its final shape ($\Delta=5,0$). The stretching ratio measured from this figure is approximately $l_f/l_i \approx 1.6$. Figures 5(b)–5(f) show the attractor computed from Eq. (9) for some sets of parameter values (a, A), strobed at $\Delta=0$. It is clear that for small dissipation [Fig. 5(f),

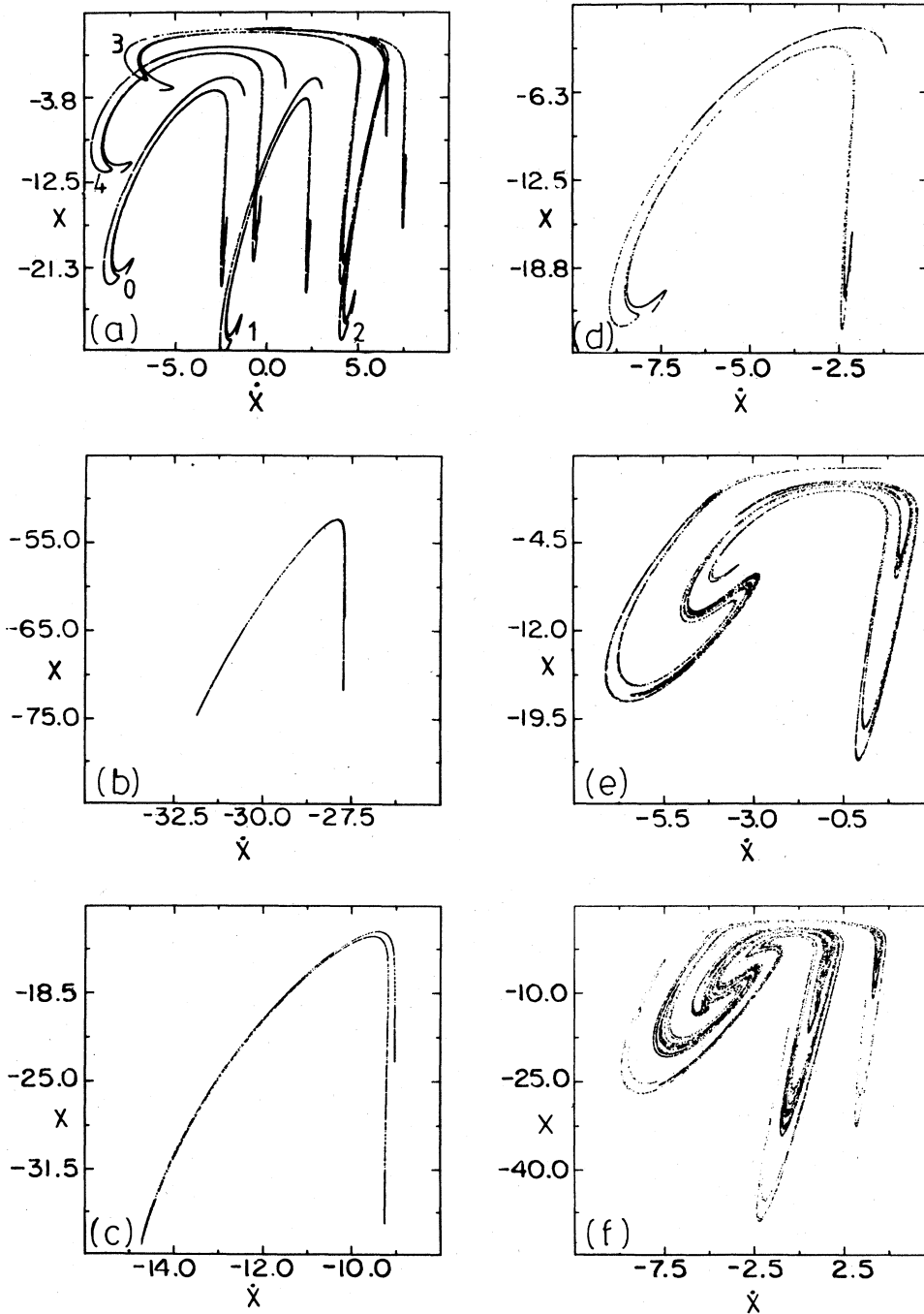


FIG. 5. Poincaré sections, x vs \dot{x} , strobed at $t=2\pi n$, $n=1,2,\dots$, from numerical solutions of Eq. (9) for various parameter sets (a, A) : (a) (0.25,5), (b) (0.75,44), (c) (0.5,5), (d) (0.25,5), (e) (0.1,2.2), (f) (0.05,2). In (a) the five sections are strobed at $t=2\pi(n+\Delta/5)$ with Δ shown on the figure.

$a=0.05$] the attractor displays self-similarity and a complex fractal structure,¹² characteristic of chaotic dynamics. However, as the dissipation is increased, the fractal structure is damped out, and for Fig. 5(b) ($a=0.75$) the attractor is essentially one dimensional and could be modeled by a one-dimensional map. Under higher resolution the attractor appears ropelike. Figure 5 sequence

demonstrates the rapid decrease of dimension of a system as dissipation is increased; this is the essence of the present belief that high-dimensional dissipative systems may be usefully represented by low-dimensional maps.

It is straightforward to make semiquantitative calculations of the fractal dimension d of the attractors in Fig. 5 using the conjecture of Kaplan and Yorke¹⁹

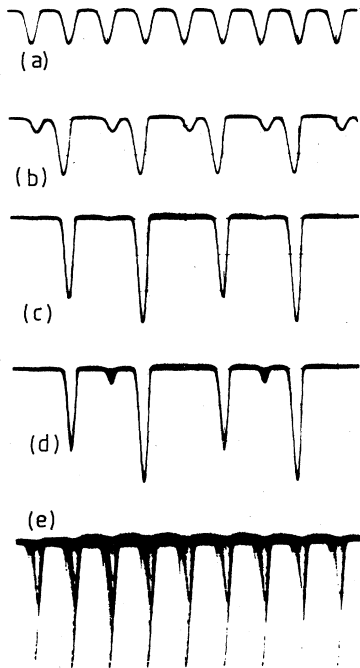


FIG. 6. Junction voltage V (vertical, arbitrary units) vs time t for driven resonator, Fig. 1, with $f=20.7$ kHz, $L=100$ mH, $R=R_C+R_0=53$ Ω , 1N4723 junction. Drive voltage (volts rms): (a) 0.318; (b) 0.601; (c) 1.332; (d) 1.575, onset of chaos; (e) 1.978, one-band chaos.

$$d = j + \frac{\sum_{i=1}^j \lambda_i}{-\lambda_{j+1}}, \quad (10a)$$

where λ_i are the characteristic Lyapunov exponents and j is the largest integer for which $(\lambda_1 + \lambda_2 + \dots + \lambda_j) > 0$. For Eq. (9), with three degrees of freedom we have $\lambda_1 > 0$, $\lambda_2 = 0$, $\lambda_3 < 0$, $j=2$, and

$$d = 2 - \frac{\lambda_1}{\lambda_3}.$$

Since nearby orbits on the attractor diverge at the rate $r(\tau) = r(0)\exp(\lambda_1\tau)$, we estimate $\lambda_1 \approx \ln(l_f/l_i)$ from the measured stretching ratio per cycle of the map ($\tau=1$). Since the total phase-space volume contraction ratio is $\exp(-a\tau) = \exp(-2\pi a)$ after one cycle of the ODE ($t=2\pi$), we set $\lambda_1 + \lambda_3 = -2\pi a$ to find

$$d = 2 + \frac{\lambda_1}{\lambda_1 + 2\pi a} \quad (10b)$$

for the dimension of the whole attractor; this is reduced by 1 for a Poincaré section. For the sections of Figs. 5(b)–5(f) the dimension is found to be 1.1, 1.15, 1.3, 1.5, and 1.7, respectively. For map contraction ratios $\exp(-2\pi a) \approx 0.1$ these attractors bear a qualitative resemblance to those observed (cf. Fig. 15), and the dimension d is comparable to that directly measured in Sec. III for driven junctions.

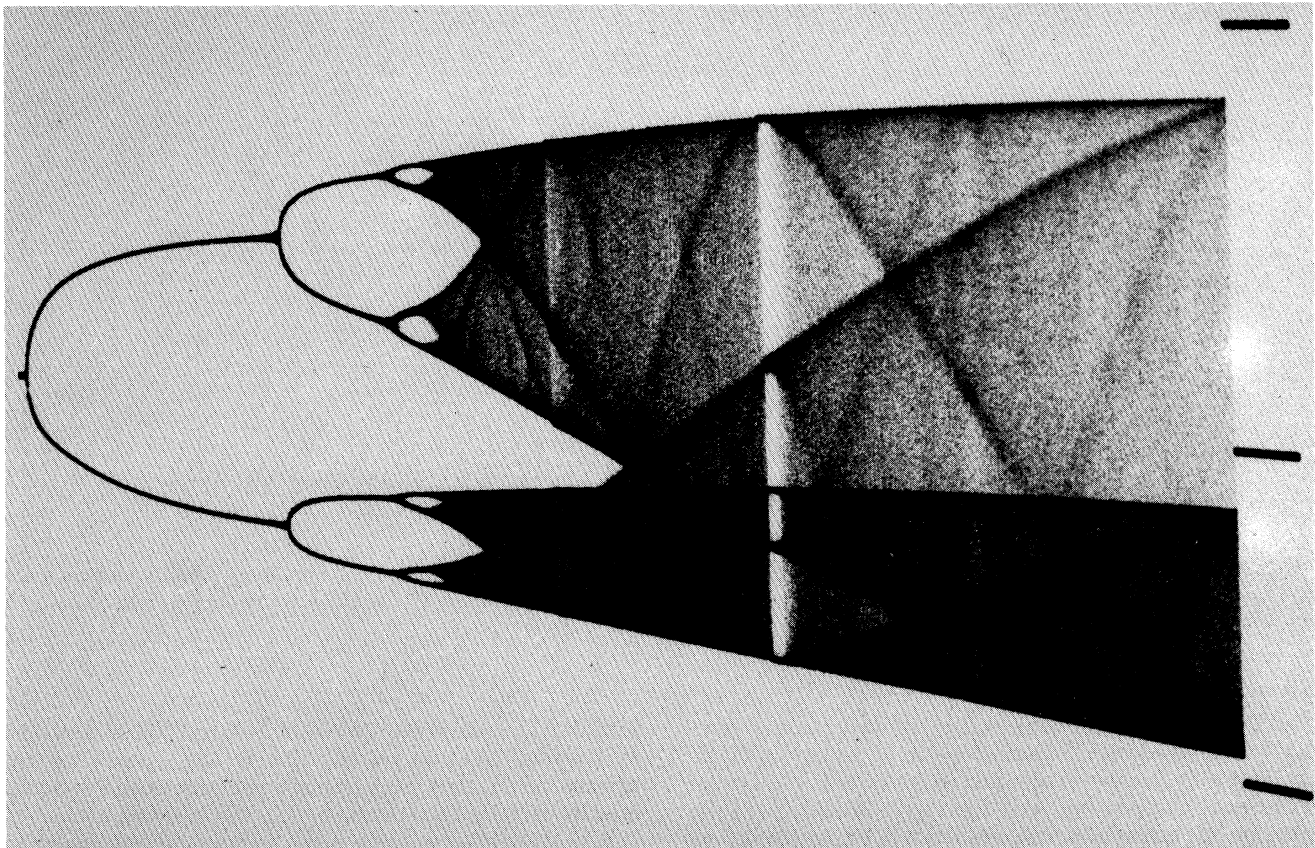


FIG. 7. Observed bifurcation diagram $[I_n]$ vertical (arbitrary units) vs drive voltage amplitude for driven p - n junction resonator, $L=470$ mH, $f=3.87$ kHz, $R=244$ Ω , 300 A p - n junction.

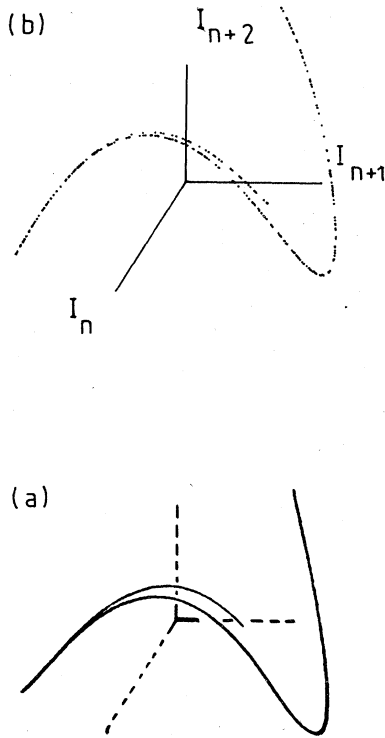


FIG. 8. (a) Observed 3D return map (arbitrary units) for driven p - n junction. (b) Computed 3D return map (arbitrary units) from Eq. (7) with $C=1.5$, $J=-0.08$.

III. EXPERIMENTAL RESULTS AND INTERPRETATION: SINGLE-JUNCTION OSCILLATOR

Bifurcation diagram. A recording of the junction voltage $V(t)$ for increasing values of the drive voltage V_{os} , Figs. 6(a)–6(c), shows a waveform of period 1,2,4, and then a nonperiodic form, 6(d), corresponding to onset of chaos. We sample and plot the set of consecutive current values $[I_n]$ separated by the driving period (the sampling phase is fixed at the current peaks in the periodic region) to obtain the bifurcation diagram of Fig. 7, showing period doubling, chaos, band merging, windows of periods 5 and 3, and veils. This is the *simplest* type of bifurcation diagram observed and is displayed by all junctions studied (approximately ten types) provided that $\omega \approx \omega_{res}$, $(2\pi/\omega) \sim \tau$, $a(q)$ is large enough, and V_{os} is not too large.

Return map. Although Fig. 7 is similar to the bifurcation diagram of the logistic map, Eq. (6), the observed return map, Fig. 8(a), is not one-dimensional and shows a structure that can be reasonably fit by Fig. 8(b), computed from the two-dimensional Hénon map, Eq. (7), with $C=1.5$, $J=-0.08$. This value of J , the phase volume contraction per cycle, is typical for junction oscillators with moderate driving.

Phase portrait and Poincaré section. Figure 9(a) shows the projection of the attractor onto the (\dot{I}, I) plane at a drive voltage for the period-3 window; the black dots are a strobed Poincaré section. Figure 9(b) is the portrait for

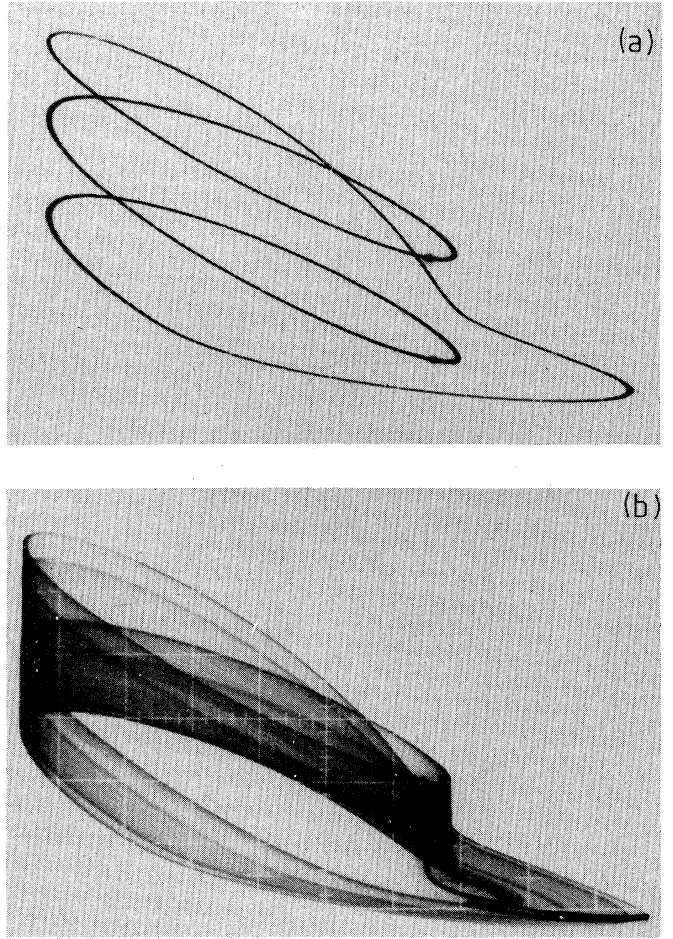


FIG. 9. (a) Observed phase portrait, I vs \dot{I} , for driven p - n junction at period-3 window: $L=100$ mH, $f=19.64$ kHz, $R=53$ Ω , 1N4723 junction, $V_{os}=3.82$ V rms; the three dark dots are a strobed Poincaré section. (b) Phase portrait and Poincaré section (dark “bent hairpin”) for same system at one-band chaos, $V_{os}=3.48$ V rms.

one-band chaos just below this window. The dark rings correspond to the veils of Fig. 7, which are successive iterates of the critical point of the map. The dark line is a Poincaré section of the attractor showing structure topologically like Fig. 8.

Period adding. If driven hard enough, junction oscillators display the bifurcation diagram of Fig. 10(a), and an average (over one cycle) junction current $\overline{I(t)} = \bar{I}$ as in Fig. 10(b). In addition to period-doubling cascades to chaos, there is a larger sequence of periodic regions of period $\dots, 3, 4, 5, \dots, N, \dots$ which we refer to as period adding, which can be physically understood as follows. We observe that \bar{I} is constant in a region of period N and furthermore that $N^{-1} \propto (\bar{I})^{-1/2}$; see data, Fig. 11. For strongly driven junctions the capacitance $C \approx C_s \propto \exp(V/\phi)$ is just proportional to the junction current I_d for large forward injection (see Sec. II), so that the average (over one cycle) capacitance $\bar{C} \propto \bar{I}_d \sim \bar{I}$. Thus the oscillator resonant frequency $\omega_{res} \propto (\bar{C})^{-1/2} \propto (\bar{I})^{-1/2} \propto N^{-1}$.

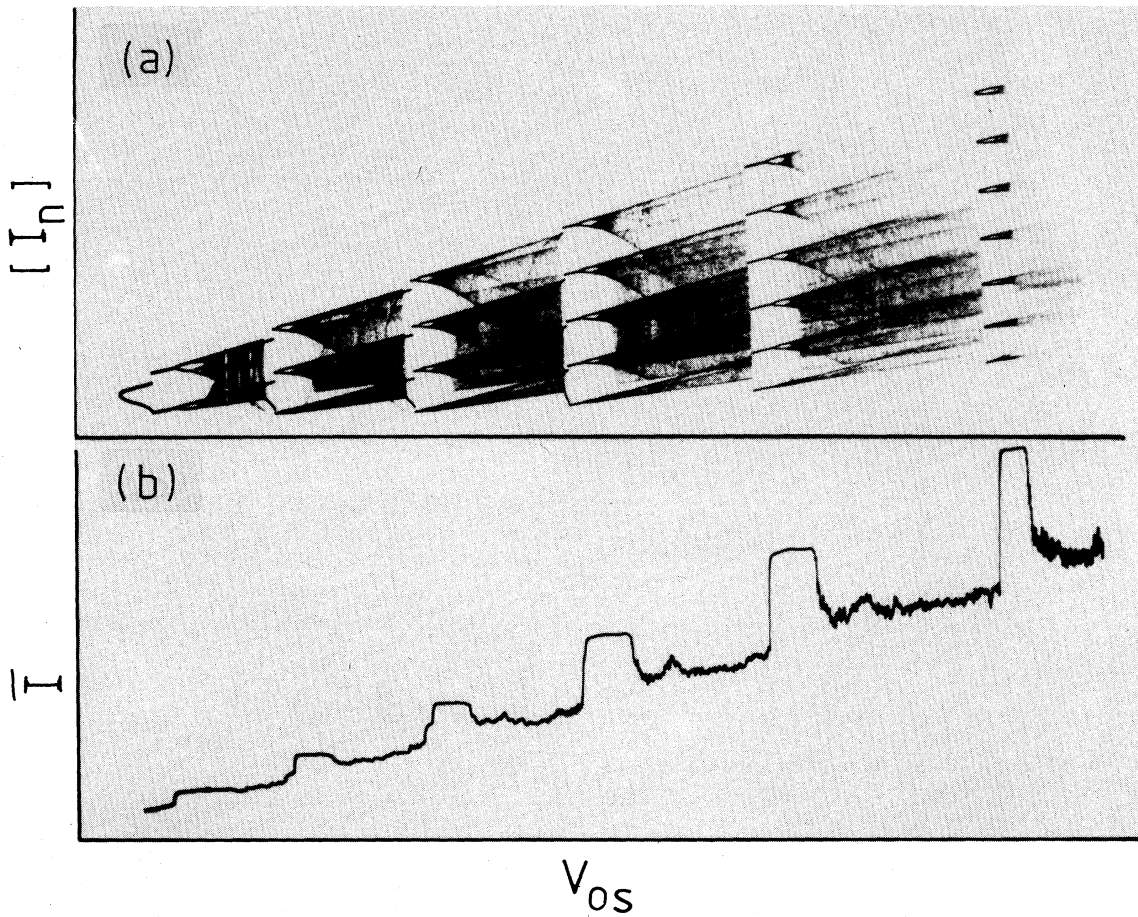


FIG. 10. (a) Bifurcation diagram $[I_n]$ vs drive voltage V_{os} (arbitrary units) for p - n junction showing period doubling and period adding (frequency locking). (b) Average junction current \bar{I} vs V_{os} , showing peaks at locked regions. $f=28$ kHz, $L=10$ mH, $R=8$ Ω , 300 A p - n junction.

That is, as this very soft spring oscillator is driven harder, it shifts its frequency down and becomes entrained or locked at successive subharmonics ω/N of the drive frequency ω . Figure 12 is a two-parameter phase diagram of the observed entrainment regions, $N:1$. The waveforms of the junction voltage V , current I , and \dot{I} for period $N=7$ are shown in Fig. 13 and can be understood from numeri-

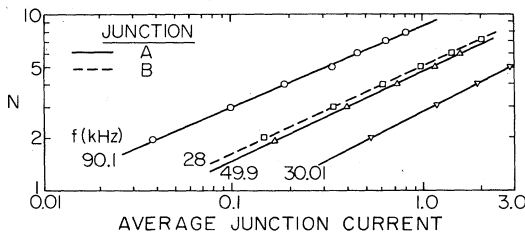


FIG. 11. Period N of locked region vs average junction current \bar{I} (in amperes) showing $N \propto (\bar{I})^{1/2}$. $L=10$ mH, $R=8$ Ω . Junction A: 1N4721. Junction B: 300 A.

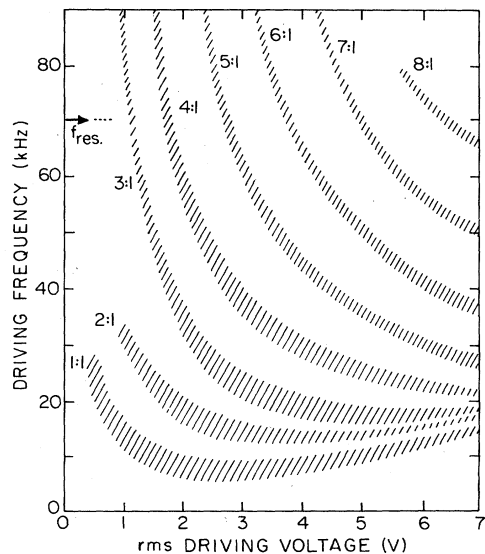


FIG. 12. Frequency of drive vs voltage at which locking of period $N:1$ occurs for driven p - n junction, $L=10$ mH, $R=8$ Ω , 1N4721 junction.

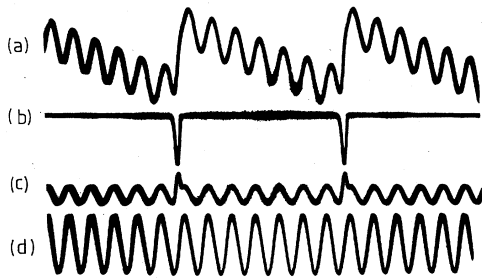


FIG. 13. Waveforms (a) $I(t)$, (b) $V(t)$, (c) $\dot{I}(t)$, and (d) drive voltage $V_0(t)$ for system of Fig. 12 at the $N=7$ locking.

cal integration of Eqs. (1).³ The observed return map, Fig. 14, for the chaotic region between period 4 and period 5 [Fig. 10(a)] shows a structure which adds one more branch as $N \rightarrow N+1$. A high-resolution Poincaré section (\dot{I}, I), Fig. 15, shows well-resolved self-similarity: four overall branches with the upper branch further divided into four sub-branches. The ratio of the tip-to-tip spreads is ~ 0.1 , which corresponds to the area contraction ratio.

Comparison to theory. As an example of theoretical modeling of behavior of a single driven junction, Fig. 16 shows a bifurcation diagram from a numerical integration of Eq. (3) with $\omega=1$ and $a=0.45$, corresponding to a contraction ratio $\exp(-2\pi a)=0.06$; this is to be compared to data, Figs. 7 and 17. Integration of Eqs. (1) with measured values of the junction parameters gives comparable results and also models period adding at large driving

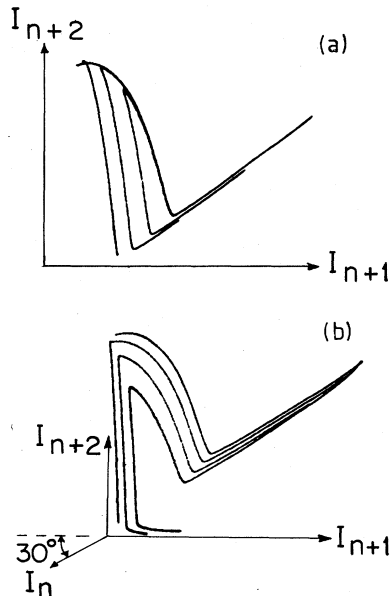


FIG. 14. (a) Two-dimensional and (b) three-dimensional return maps for the system of Fig. 10 in the chaotic region between $N=4$ and 5.

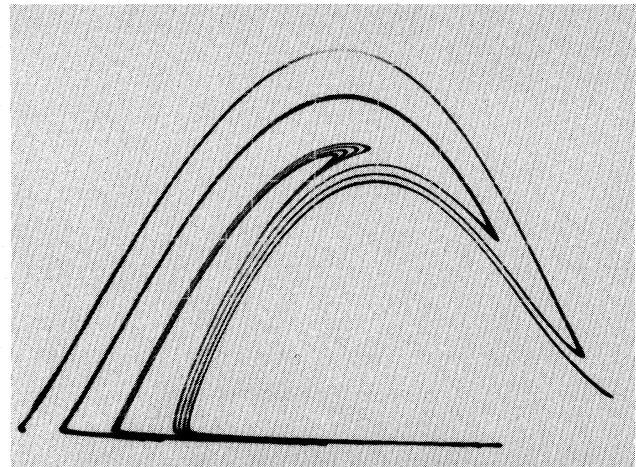


FIG. 15. Poincaré section, I vs \dot{I} , showing self-similarity and fractal structure. $L=10$ mH, $f=76$ kHz, $R=43$ Ω , 1N4721 junction.

voltage. Period adding can also be reasonably modeled by this two-dimensional map of the form of Eq. (8):

$$x_{n+1} = [x_n + 1 - S(x_n)] - S(A\{1 - [S(-x_n)]^2\}) - y_n, \tag{11a}$$

$$y_{n+1} = Bx_n, \tag{11b}$$

$$S(x) = \frac{1}{2}[x + (x^2 + 0.1)^{1/2}]. \tag{11c}$$

Figure 18 is a bifurcation diagram computed from Eqs. (11) with $B=0.1$ and using A as the control parameter; it is a reasonable fit to the data of Fig. 10(a), except for the

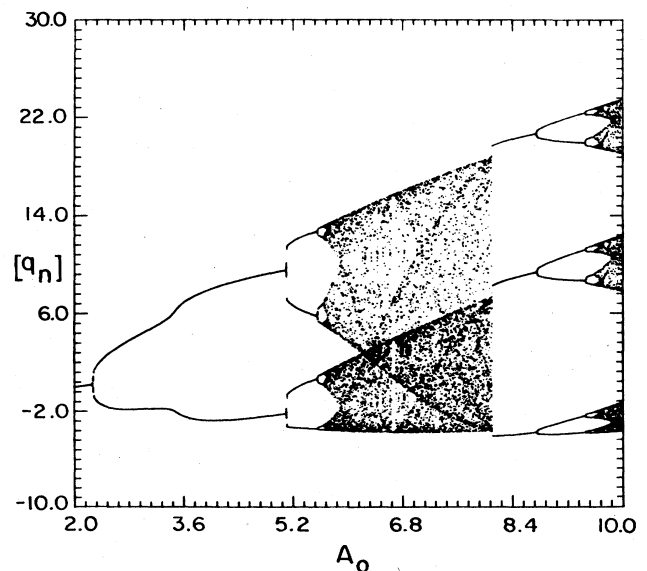


FIG. 16. Computed bifurcation diagram $[q_n]$ vs A_0 from Eq. (3) with $\omega=1$, $a=0.45$; compare to data, Fig. 17.

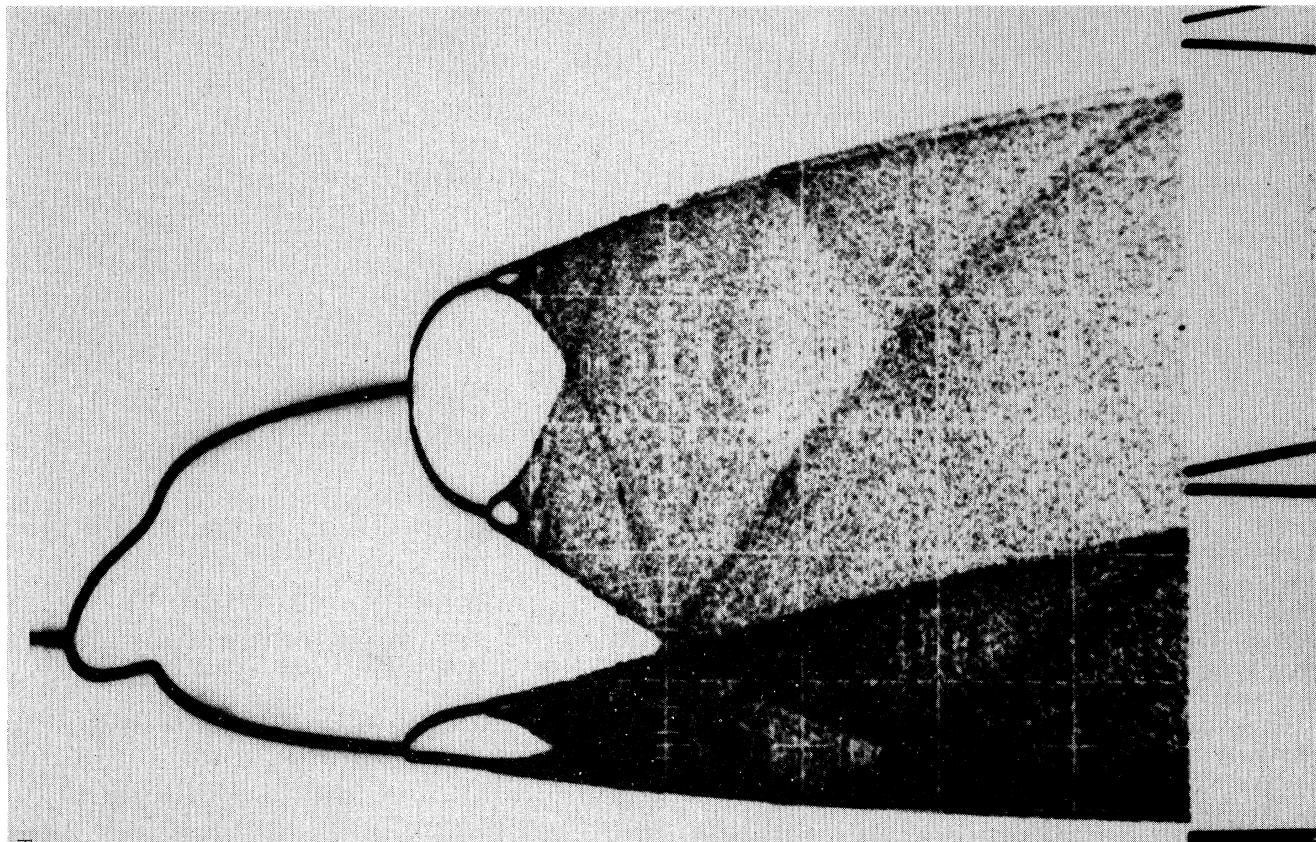


FIG. 17. Measured bifurcation diagram, $[I_n]$ vs V_{os} (horizontal, arbitrary units) for driven junction. $L=100$ mH, $R=53$ Ω , $f=20.3$ kHz, 1N4723 junction.

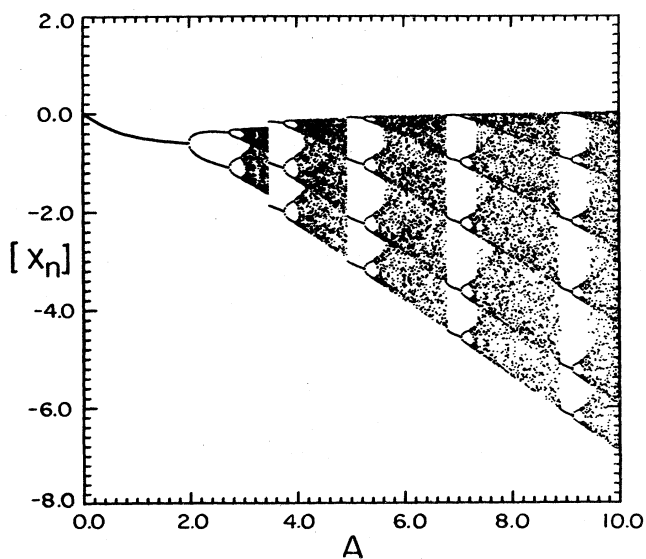


FIG. 18. Bifurcation diagram: $[X_n]$ vs A computed from Eq. (11) with $B=0.1$ showing period doubling, period adding, and hysteresis, with overall behavior similar to the data of Fig. 10.

$2 \rightarrow 2$ jump at low voltages, a subtle phenomena sensitive to system parameters and better explained by Fig. 16.

Phase diagram. An overview of junction oscillator behavior for the system used for Fig. 17 is provided by the two-parameter phase diagram of Fig. 19: a plot of the boundaries between various periodic and chaotic regions as a function of driving voltage V_{os} and frequency $f = \omega/2\pi$. The junction resonance occurs at $f_{res} = 20$ kHz. Increasing V_{os} upward along a line of constant frequency f_{res} yields the simplest bifurcation sequence: periods 1,2,4,8, ..., chaos, ..., two-band chaos C2, one-band chaos C1, period-3 window (with hysteresis \uparrow, \downarrow), period 6, three-band chaos C3, and one-band chaos C1 (interior crisis). At higher drive voltage there begins a period-adding sequence—see the phase diagram of Fig. 12. Moving upward along $f=34$ kHz in Fig. 19 gives a sequence 1,2,4,8,4,2,1 without chaos. Increasing frequency at $V_{os}=2$ V gives a sequence 1,2,4,8, ..., chaos, ..., 8,4,2,1. This makes clear why such a wide variety of bifurcation diagrams are observed, e.g., Fig. 20 showing reverse bifurcation.

To compare the observed phase diagram of Fig. 19 with our model we numerically integrated Eq. (3) for $a=0.45$ for the two control parameters $0 \leq A_0 < 20$, $0.4 \leq \omega \leq 3$, with the resulting theoretical phase diagram of Fig. 21,

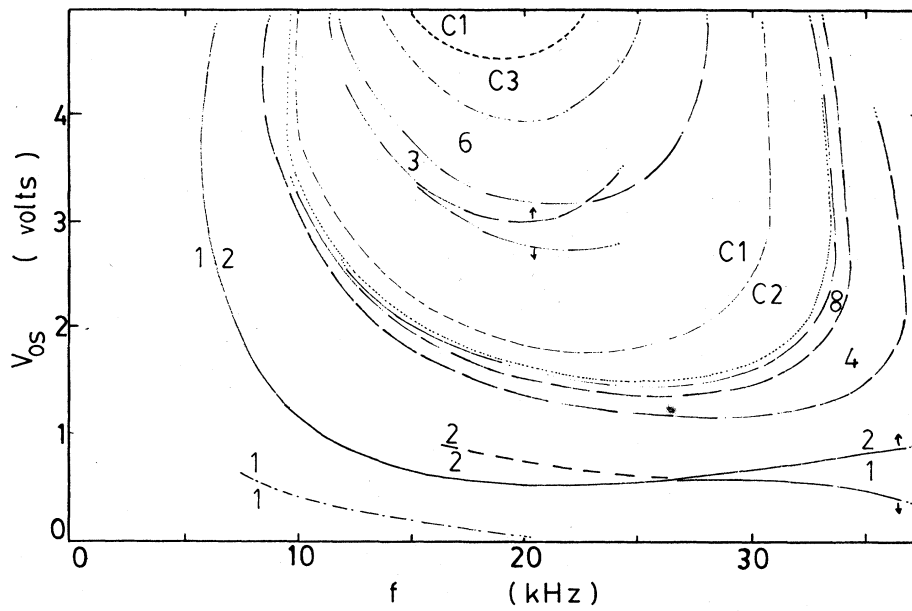


FIG. 19. Phase diagram: Drive voltage V_{os} vs frequency f of junction oscillator showing boundaries between periods 1,2,4,8; threshold for chaos; two-band chaos $C2$; one-band chaos $C1$; periods 3,6; three-band chaos $C3$; $C1$; hysteresis: (\uparrow, \downarrow); 1:1 and 2:2 jump bifurcations. $L = 100$ mH, $R = 53 \Omega$, 1N4723 junction.

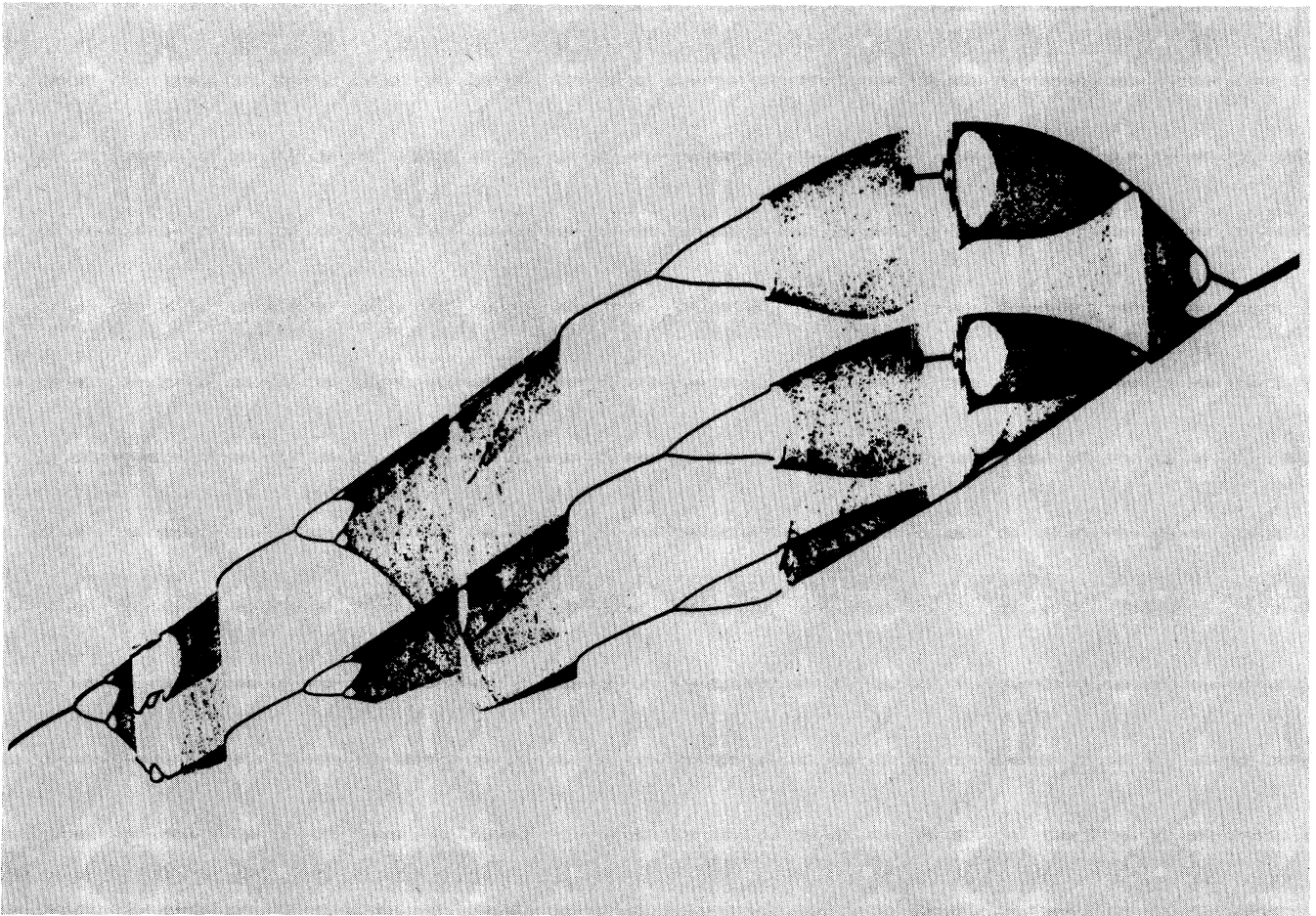


FIG. 20. Observed bifurcation diagram $[I_n]$ vs V_{os} (horizontal, arbitrary units) for driven junction, $f = 11.79$ kHz, $L = 10$ mH, $R = 8 \Omega$, 300 A junction.

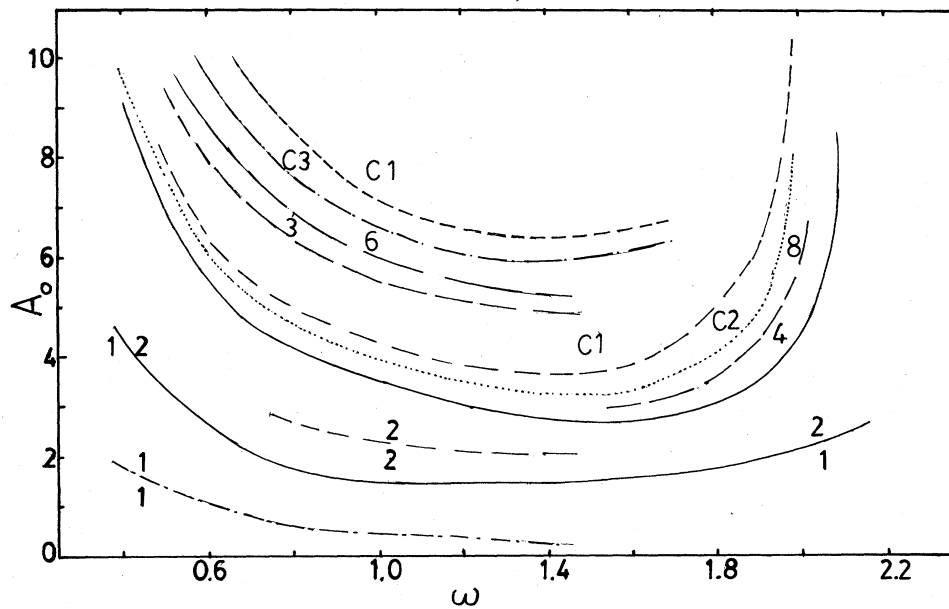


FIG. 21. Computed phase diagram, A_0 vs ω , from integration of Eq. (3) with $a=0.45$, showing boundaries between periods 1,2,4,8; two-band chaos C2; one-band chaos C1; periods 3,6; three-band chaos C3; C1; and 1:1 and 2:2 jump bifurcations.

which shows a satisfactory agreement with the data by making the usual correspondences $(A_0, \omega) \rightarrow$ (voltage, frequency of drive oscillator). That the theoretical diagram does not show sharply increasing values of drive voltage to cross boundaries on either side of resonance is probably due to use of a constant value $a(q) \rightarrow a$ in Eq. (3). Figures

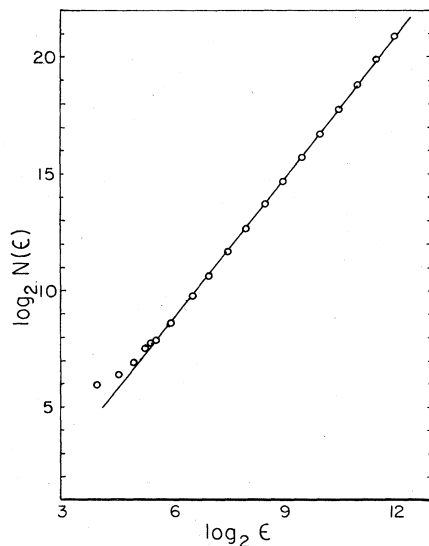


FIG. 22. Plot of $\log_2 \overline{N(\epsilon)}$ vs $\log_2 \epsilon$ for embedding dimension $D=6$ giving line of slope $d=2.04 \pm 0.03$, the fractal dimension of the attractor for driven p - n junction in chaotic region just below period-3 window. $L=100$ mH, $R=77 \Omega$, $f=19.881$ kHz, $V_{os}=3.105$ V rms, 1N4723 junction.

19 and 21 both show a period-1 \rightarrow period-1 bifurcation, and a period-2 \rightarrow period-2 bifurcation. These are observed (Fig. 17) and predicted (Fig. 16) on bifurcation diagrams and are examples of the jump phenomena for driven nonlinear oscillators; cf. Fig. 4.

*Fractal dimension of attractor.*²⁰ The assumed equations of motion, Eqs. (1), contain three dynamical variables.²¹ We suppose the motion can be described in a three-dimensional phase space, neglecting the possibility (Sec. II) that the system has a higher-dimensional memory from diffusive motion of injected charge. We test this supposition below. Since the system has negative divergence of phase-space flow, the attractor must have zero volume and thus must have dimension d less than three; furthermore, to be chaotic the dimension must be greater than two.¹² So we expect the dimension to be a fractal, $2 < d < 3$. It is of interest to measure d , and we do so as follows.^{22,23} We record a data set of $q=96\,000$ values of the junction current $I(t)$ using a fast 12-bit (binary digit) analog-to-digital converter and a Digital Equipment Corporation LSI-11/23 minicomputer. By strobing the converter asynchronously with respect to the driving period, we collect data from the whole attractor rather than from a fixed Poincaré section. From the data set $\{A_0, A_1, \dots, A_n, \dots, A_q\}$ we construct q vectors $\mathbf{B}_n = (A_n, \dots, A_{n+D-1})$ in a D -dimensional phase space, the "embedding" space. We measure the number of points on the attractor $N(\epsilon)$ which are contained in a D -dimensional hypersphere of radius ϵ centered on a particular \mathbf{B}_n . One expects scaling of the form

$$N(\epsilon) \propto \epsilon^d,$$

where d is the attractor dimension. Thus a plot of

$\log_{10}\overline{N(\epsilon)}$ versus $\log_{10}\epsilon$ is expected to have a slope d , where $\overline{N(\epsilon)}$ is the average for hyperspheres centered on many different \mathbf{B}_n . This procedure can be carried out for consecutive values of $D=2,3,4,\dots$, to ensure that the embedding dimension is chosen sufficiently large (important if dimension of phase space is not known) and to discriminate against high-dimensional stochastic noise, not of deterministic origin. The resulting plot for $D=6$ is shown in Fig. 22 for the system of Fig. 17 with V_{os} set for a one-band chaotic attractor just below the period-3 window. From the slope we find $d=2.04\pm 0.03$. The same slope was found for $D=4$, i.e., the slope converged for $D\geq 4$. Data were also taken for a Poincaré section by strobing the converter synchronously with the drive; these data gave a value $d_{PS}=1.06\pm 0.02$, less by unity than d , as expected. In summary, these fractal dimension measurements show that $2 < d < 3$ and are consistent with Eqs. (1) and (3). However, they do not exclude the possibility that the system has a higher-dimensional phase space, since sufficient dissipation could reduce d to the value measured.

To summarize this section on a single-junction resonator we compare various theoretical models in their ability to predict observed behavior. The simplest, the logistic map, Eq. (6), while yielding a bifurcation diagram superficially like those observed, cannot explain hysteresis, period adding, nor the fractal structure. The Henon map, Eq. (7), with a Jacobian of $J\sim 0.1$, can model the return map at moderate drive, the bifurcation diagram with hysteresis, but not the period adding. The two-dimensional (2D) map of Eq. (11), of form tailored to the junction characteristics, can model period adding. Differential equations, Eqs. (1) and (3), with more parameters, seem to be the best models and can even model the phase diagram in parameter space. Brorson *et al.*⁴ have accurately modeled behavior using an equation similar to Eq. (3) with ten measured input parameters.

IV. TWO COUPLED JUNCTION OSCILLATORS

A. Introduction

Having well characterized theoretically and experimentally the single driven p - n junction resonator, one is prepared to predict and to observe the behavior when two or more are coupled together and driven. Coupled nonlinear oscillators or modes are central to the understanding of extended systems, e.g., a line of lattice oscillators or coupled plasma-wave modes. A system of two oscillators has the possibility to make a Hopf bifurcation to a second incommensurate frequency and follow a quasiperiodic route to chaos, in addition to period doubling and intermittency. Such routes, first discussed by Ruelle and Takens,²⁴ are not yet really understood.

Equations of motion; ODE model. It is possible to couple two identical junction resonators in various ways and we discuss only these two. (i) Resistive coupling: in Fig. 1 connect A to B ; the two resonators are coupled through their currents which flow in a common coupling resistance R_C to the driving oscillator. (ii) Line coupling: connect B to D and set $R_C=0$; the driving oscillator

drives the lower resonator, which excites the upper resonator in a configuration modeling a nonlinear transmission line.

For resistive coupling, the coupled equations of motion obtained from Kirchoff's laws and Eqs. (3) and (4) are

$$\ddot{q}_1 + \beta[b\dot{q}_1 + r(\dot{q}_1 + \dot{q}_2)] - f(q_1) = A_0 \sin(\omega t), \quad (12a)$$

$$\ddot{q}_2 + b\dot{q}_2 + r(\dot{q}_1 + \dot{q}_2) - f(q_2) = A_0 \sin(\omega t), \quad (12b)$$

where $r \equiv R_C/L$ is the coupling coefficient, $b(q) = (1/C(q))(\partial I_D/\partial V) \approx b$, $b+r=a$ in Eq. (3), $f(q)$ is given by Eq. (4b), and a small term $rI_d(q_2)$ is neglected in Eq. (12a) and a term $rI_d(q_1)$ neglected in Eq. (12b). The factor $\beta \lesssim 1$ is introduced to take into account small differences in the two p - n junctions. From the form of Eq. (12) we see that the coupling is through the currents via the common resistance R_C .

For line coupling the coupled equations are

$$\ddot{q}_1 + a\dot{q}_1 - 2f(q_1) + f(q_2) = A_0 \sin(\omega t), \quad (13a)$$

$$\ddot{q}_2 + a\dot{q}_2 - f(q_2) + f(q_1) = 0, \quad (13b)$$

where a and $f(q)$ are given by Eq. (4). The coupling is through the $f(q)$ term which is essentially the potential across the junction, corresponding to the restoring force.

Map models. In the same way that a two-dimensional map [Eq. (8) and Eqs. (11)] was used to model a single junction, including its specific characteristics, we now model two coupled junctions by taking two two-dimensional maps and adding a simple linear coupling term to each:

$$z_{n+1} = f(\lambda, z_n) - y_n + CZ_n, \quad (14a)$$

$$y_{n+1} = Jz_n, \quad (14b)$$

$$Z_{n+1} = f(\lambda', Z_n) - Y_n + C'z_n, \quad (14c)$$

$$Y_{n+1} = JZ_n. \quad (14d)$$

For simplicity, choose $|C'| = C$; this still leaves open two choices, $C' = C$ or $C' = -C$. From linearization about a bifurcating fixed point we find, for $C' = C$, real eigenvalues of the matrix and a period-doubling bifurcation initially. For $C' = -C$, the eigenvalues are complex, leading to a Hopf bifurcation initially. The experiments below find that resistive coupling gives first a period-doubling bifurcation, while line coupling gives a Hopf bifurcation first. We take the following specific form of Eq. (14) to model two coupled junctions:

$$z_{n+1} = \gamma[z_n + 1 - S(z_n)] - S(A\{1 - [S(z_n)]^2\}) - y_n + CZ_n, \quad (15a)$$

$$y_{n+1} = Jz_n, \quad (15b)$$

$$Z_{n+1} = \gamma[Z_n + 1 - S(Z_n)] - S(bA\{1 - [S(Z_n)]^2\}) - Y_n + C'z_n, \quad (15c)$$

$$Y_{n+1} = JZ_n, \quad (15d)$$

$$S(z) = 0.5[z + (z^2 + 0.1)^{1/2}] \quad (15e)$$

with $b \approx 1$ an asymmetry parameter; $C' = +C$ for resistive

coupling; $C' = -C$ for line coupling; A is control parameter; and $\gamma < 1$ so that map is globally stable and attracting (typically $\gamma = 0.5$ for resistive coupling and $\gamma = 0.85$ for line coupling).

Coupled logistic maps. A simpler map model is obtained from Eqs. (15) for very dissipative systems by taking $J=0$ and a simple quadratic form for the nonlinearity; this yields two linearly coupled logistic maps

$$z_{n+1} = \lambda z_n(1 - z_n) + \epsilon y_n, \quad (16a)$$

$$y_{n+1} = \lambda y_n(1 - y_n) + \epsilon' z_n, \quad (16b)$$

where λ is the drive parameter and ϵ is the coupling parameter. This two-dimensional map has been studied in

detail by several authors,²⁵⁻²⁹ particularly for the case $\epsilon = \epsilon'$. A phase diagram in (λ, ϵ) parameter space has been computed^{25,28} showing the domains of period-doubling and symmetry-breaking bifurcations, Hopf bifurcation to quasiperiodicity, regions of entrainment or locking to a rational ratio of the two frequencies, and chaos. For all values of $\epsilon = \epsilon'$, one first finds period doubling to period 2, then a Hopf bifurcation as λ is increased. Other generic behavior studied includes oscillation of the torus,³⁰ crises,²⁹ and intermittency between locked and quasiperiodic states. The chaotic attractors have a somewhat characteristic appearance of folded rugs or strange animals.

Sine circle map. This map has been used to model the

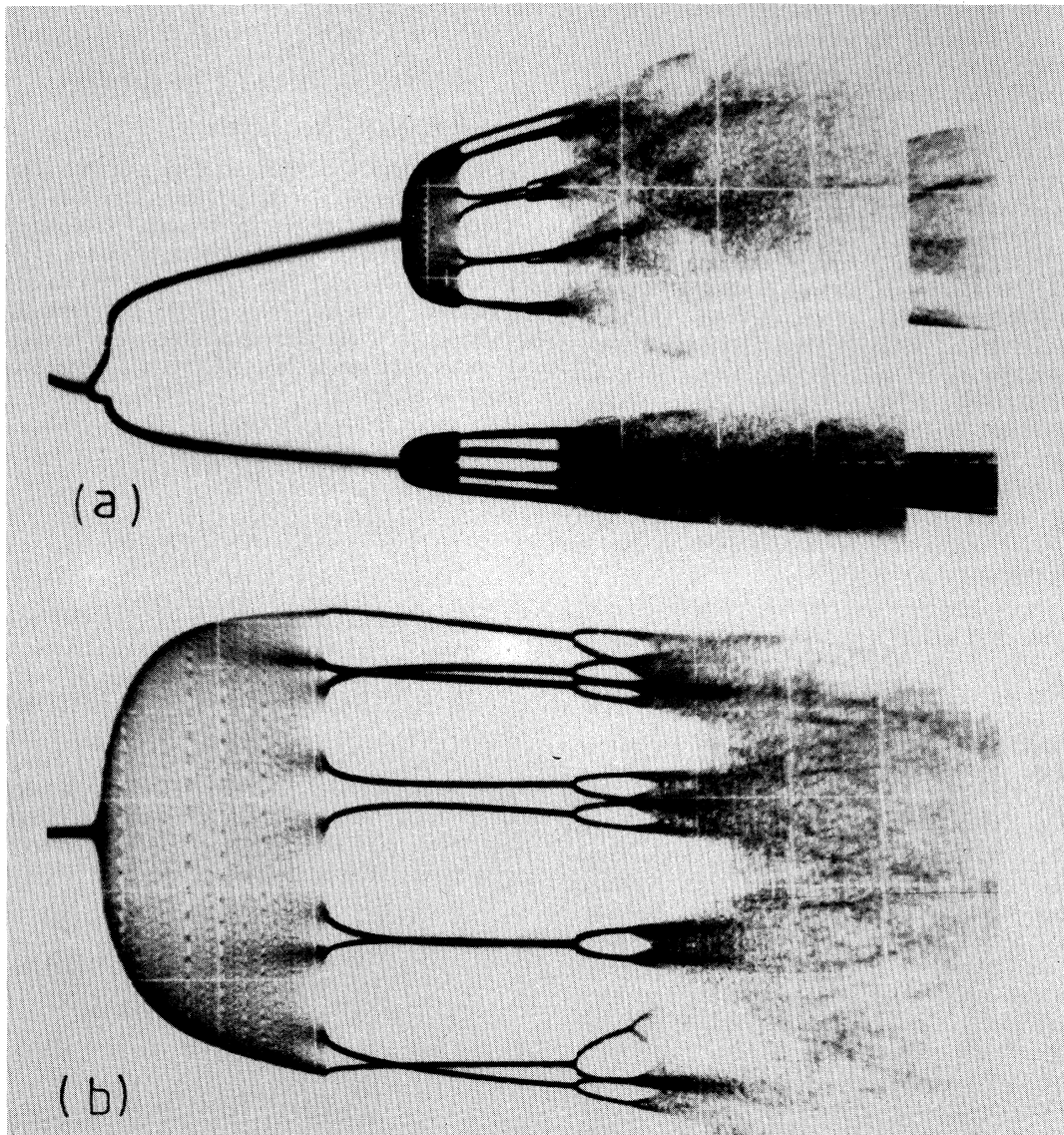


FIG. 23. (a) Bifurcation diagram $[I_n]$ vs V_{os} for two identical resistively coupled junctions, showing period doubling, Hopf bifurcations, and chaos. (b) Enlarged bifurcation diagram $[V_n]$ vs V_{os} of upper center section of (a), showing Hopf bifurcation, entrainment, doubling, chaos. $L = 100$ mH, $R_C = 1200$ Ω , $f = 27.127$ kHz, 1N4723 junction.

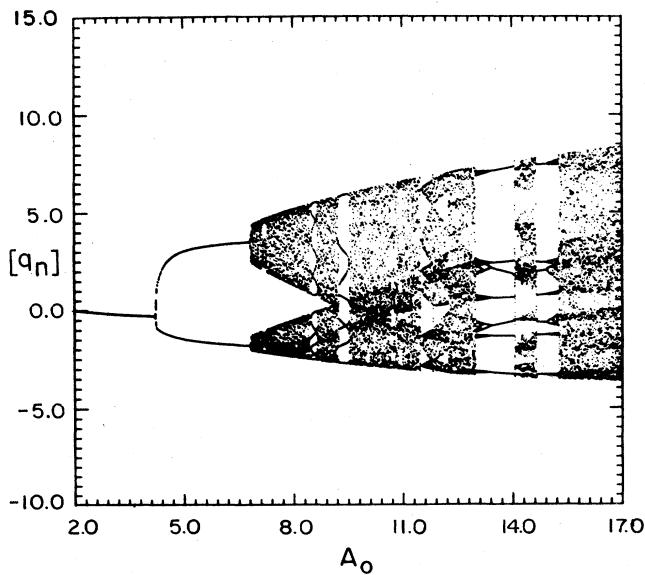


FIG. 24. Computed bifurcation $[q_n]$ vs A_0 from Eq. (12) with $\beta = \frac{19}{20}$, $b = 0.45$, $r = 0.6$, $\omega = 1.5$.

phase motion of two coupled oscillators:

$$\theta_{n+1} = \theta_n + \Omega - (\kappa/2\pi)\sin(2\pi\theta_n), \quad (17)$$

where the parameter Ω is the frequency ratio in the absence of the last term and κ is the drive (or coupling) parameter. This equation has been abundantly studied.^{31,32} In the phase diagram in κ, Ω parameter space, for $\kappa < 1$, there are entrainment horns at all rational values of Ω , and quasiperiodic orbits in between. These "Arnol'd tongues"³³ merge at $\kappa = 1$ at onset of chaos, accompanied by hysteresis and intermittency; period doubling can occur at $\kappa > 1$. Universal behavior at $\kappa = 1$ includes scaling of the power spectra for rotation numbers equal to the reciprocal of the golden mean;³¹ and a fractal dimension $D = 0.87 \dots$ for the quasiperiodic orbit set.³² Equation (17) is the simplest model to predict entrainment horns, observed below in coupled junctions.

B. Resistive coupling: Experiments and interpretation

Two junction resonators, identical to that used in Fig. 17, were resistively coupled as in Fig. 1 and driven at frequency $f = f_1 = 27$ kHz. The observed bifurcation dia-

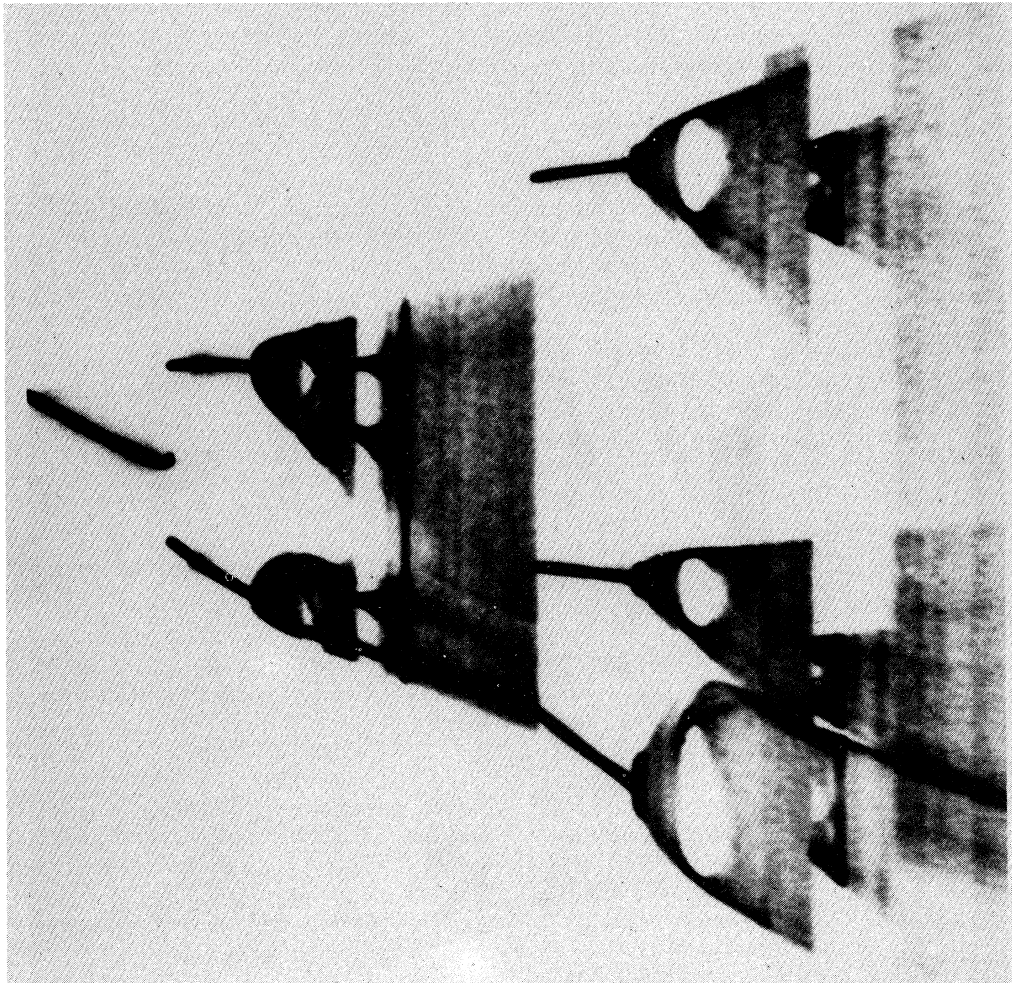


FIG. 25. Measured bifurcation diagram $[J_n]$ vs V_{os} for two identical resistively coupled junctions, $L = 8.2$ mH, $R_C = 100 \Omega$, $f = 120$ kHz, 1N4723 junction.

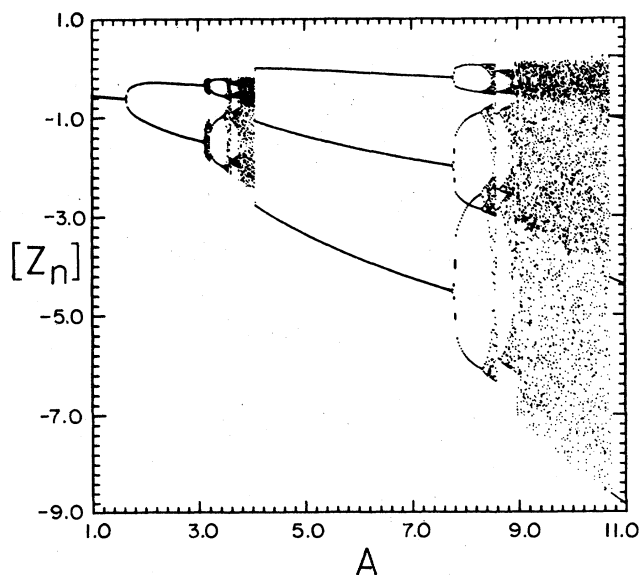


FIG. 26. Bifurcation diagram $[Z_n]$ vs A computed from Eq. (15) for two resistively coupled junctions, with $\gamma=0.5$, $b=0.95$, $C'=C=0.05$, $J=0.1$.

gram is shown in Fig. 23(a). After period doubling to $f_1/2$ there occurs a Hopf bifurcation to a second, incommensurate frequency, $f_2 \approx 0.22f_1$, followed by narrow locked regions [see expanded diagram, Fig. 23(b)] and then a wide locked region with winding number $\rho = f_1/f_2 = \frac{9}{2}$. Then follows period doubling to chaos, an abrupt jump in attractor size, further locking, etc. (not shown). This figure shows the clear distinction in a bifurcation diagram between period doubling and Hopf bifurcations. To compare this data to a model, we use the coupled ODE's, Eqs. (12), to compute the bifurcation diagram of Fig. 24, using $\beta = \frac{19}{20}$, damping constant $b=0.45$, coupling constant $r=0.6$, and relative drive frequency $\omega=1.5$. The model agrees with the data in showing first a period-doubling bifurcation, then a Hopf bifurcation with many narrow lockings. However, this model does not then show a wide locking and period doubling to chaos but rather more lockings, becoming wider at larger A_0 . It would appear that to find ODE models that give detailed agreement is more difficult for $N=2$ than $N=1$ oscillators.

Figure 25 is another experimental bifurcation diagram taken under different experimental parameters corresponding to weaker coupling, $R_C = 100 \Omega$. The data show period doubling, Hopf bifurcation, locking, jump to period 4, chaos, period 3, Hopf bifurcation, rough period 6, chaos, crisis (jump), etc. We compare this data to a different model: Fig. 26 shows a bifurcation diagram computed from the iterative map model, Eq. (15), with $\gamma=0.5$, asymmetry parameter $b=0.95$, and coupling $C'=+C=0.05$. The qualitative agreement with Fig. 25 is surprisingly good: The sequence of events is close to that of the data. Both the data and the model show first a period-doubling bifurcation, a Hopf bifurcation, period 4, chaos, and then period 3. The data then show a Hopf bi-

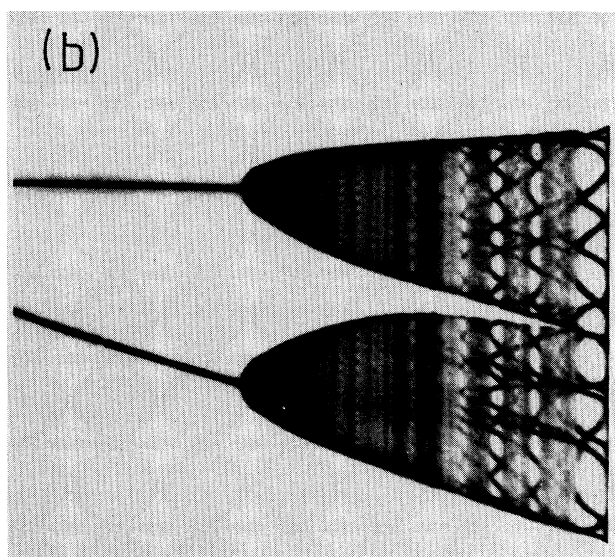
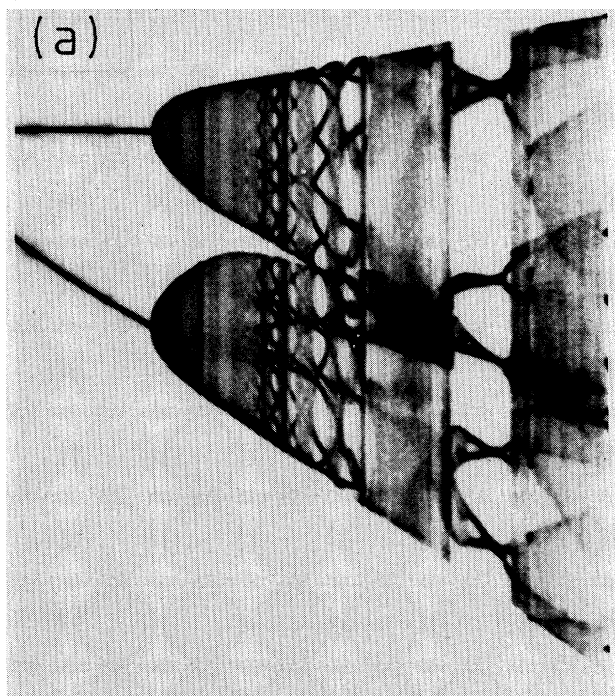


FIG. 27. (a) Observed bifurcation diagram $[I_n]$ vs V_{os} for system of Fig. 25 with coupling increased to $R_C = 1200 \Omega$. Compare to model, Fig. 28(a). (b) Expanded view of center section of (a).

furcation and a period-6 band, whereas the model does not show this Hopf bifurcation but rather a clear period 6.

Figure 27 is a diagram for the same system as in Fig. 25 but with the coupling resistance increased to $R_C = 1200 \Omega$. Figure 28(a) is a diagram computed from Eq. (15) with coupling $C'=C=0.6$; it compares well with the data of Fig. 27(a). Figure 28(b) is a high-resolution expansion of the diagram at $2 \rightarrow 1$ band merge. There are 21 lines resolved, to be compared to approximately the

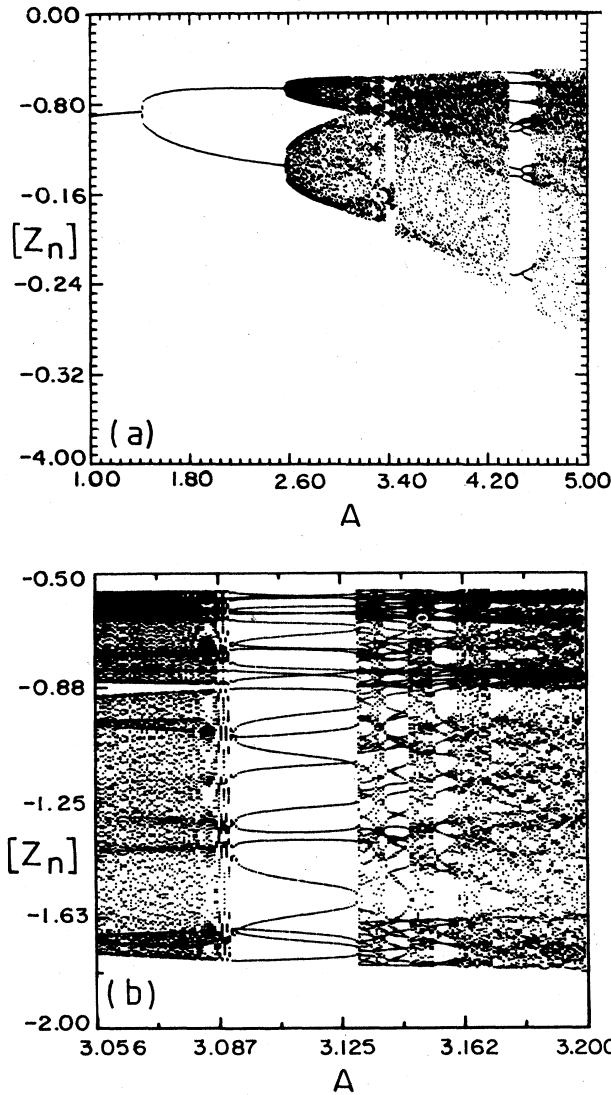


FIG. 28. (a) Bifurcation diagram $[Z_n]$ vs A computed from Eq. (15) with $\gamma=0.5$, $b=0.95$, $J=0.1$, $C=C'=0.6$. (b) Blow-up of 1 \rightarrow 2 band merge region of (a).

same number in the data, Fig. 27(b). This is probably fortuitous since we do not expect such detailed agreement with the model.

In summary, for two resistively coupled junction resonators we find qualitative agreement with bifurcation diagram data using the ODE model, Eq. (12), and somewhat better agreement with the four-dimensional map model, Eq. (15). We note that bifurcation diagrams computed from coupled logistic maps (Ref. 28, Fig. 2 for coupling $\epsilon=0.06$; Ref. 25, Fig. 4 for coupling $d=0.1$) also bear a qualitative resemblance to our data.

Phase diagram. An overview of the behavior of two coupled junction resonators is given by the phase diagram in Fig. 29 in (V_{os}, f_1) parameter space (not shown is a bifurcation from period 1 to period 2 along a line similar to that in Fig. 19 for one resonator). Along the boundary of

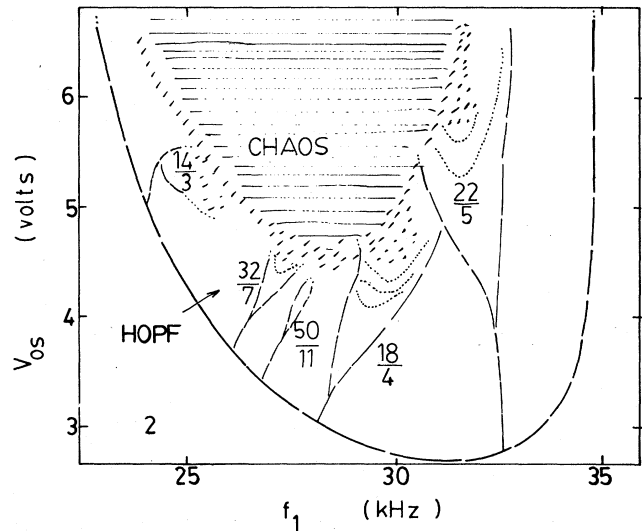


FIG. 29. Observed phase diagram for two resistively coupled junction oscillators: in parameter space, drive voltage V_{os} and drive frequency f_1 , the heavy line is the boundary of a Hopf bifurcation from $f_1/2$ to quasiperiodicity, with new frequency f_2 . Entrainment horns are labeled by $P/Q=f_1/f_2$. Period doubling (dotted lines) occurs within horn.

the Hopf bifurcation the frequency ratio $\rho=f_1/f_2$ varies continuously from 4.732 18 (upper left of Fig. 29) to 4.344 42 (upper right). Where ρ tends to a rational number P/Q , a point of resonance, there emerges from the boundary an entrainment horn or Arnol'd tongue.³³ There are many other narrow horns not shown. Period doubling to chaos occurs within the horns,³⁴ as shown. Where two horns overlap there is hysteresis and intermittency between the two attractors, leading to chaos: one can say that this "confusion leads to chaos."³⁵ The re-

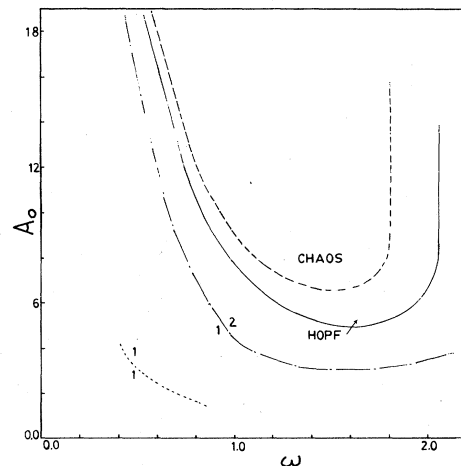


FIG. 30. Phase diagram, A_0 vs ω , for two resistively coupled junctions computed from Eq. (12) with $\gamma=19/20$, $b=0.45$, $r=0.6$, showing boundary of 1:1 jump bifurcation, 1:2 period doubling, Hopf bifurcation, and approximate region of chaos.

gions of chaos (however reached: by period doubling, by overlap of horns, by following a “true” quasiperiodic route along an irrational rotation number) are widespread but fall roughly in the shaded region shown. We note that this phase diagram for two driven passive resonators is qualitatively similar to a much more detailed phase diagram for a driven active nonlinear oscillator.^{36,37} In both cases the entrainment horns are very roughly modeled by Eq. (17).

To test the ODE model we have used Eqs. (12) to compute the phase diagram of Fig. 30 which shows reasonably well the principal features of the data, Fig. 29, including the boundaries of the period doubling and Hopf bifurcations and the region of chaos.

Breakup of the torus. From the five-dimensional phase space of two driven coupled resonators (e.g., $I_1, V_1, I_2, V_2, \theta$) we select the space (I_2, V_1, θ) to examine experimentally and look at the $(I_2(t), V_1(t))$ phase portrait.

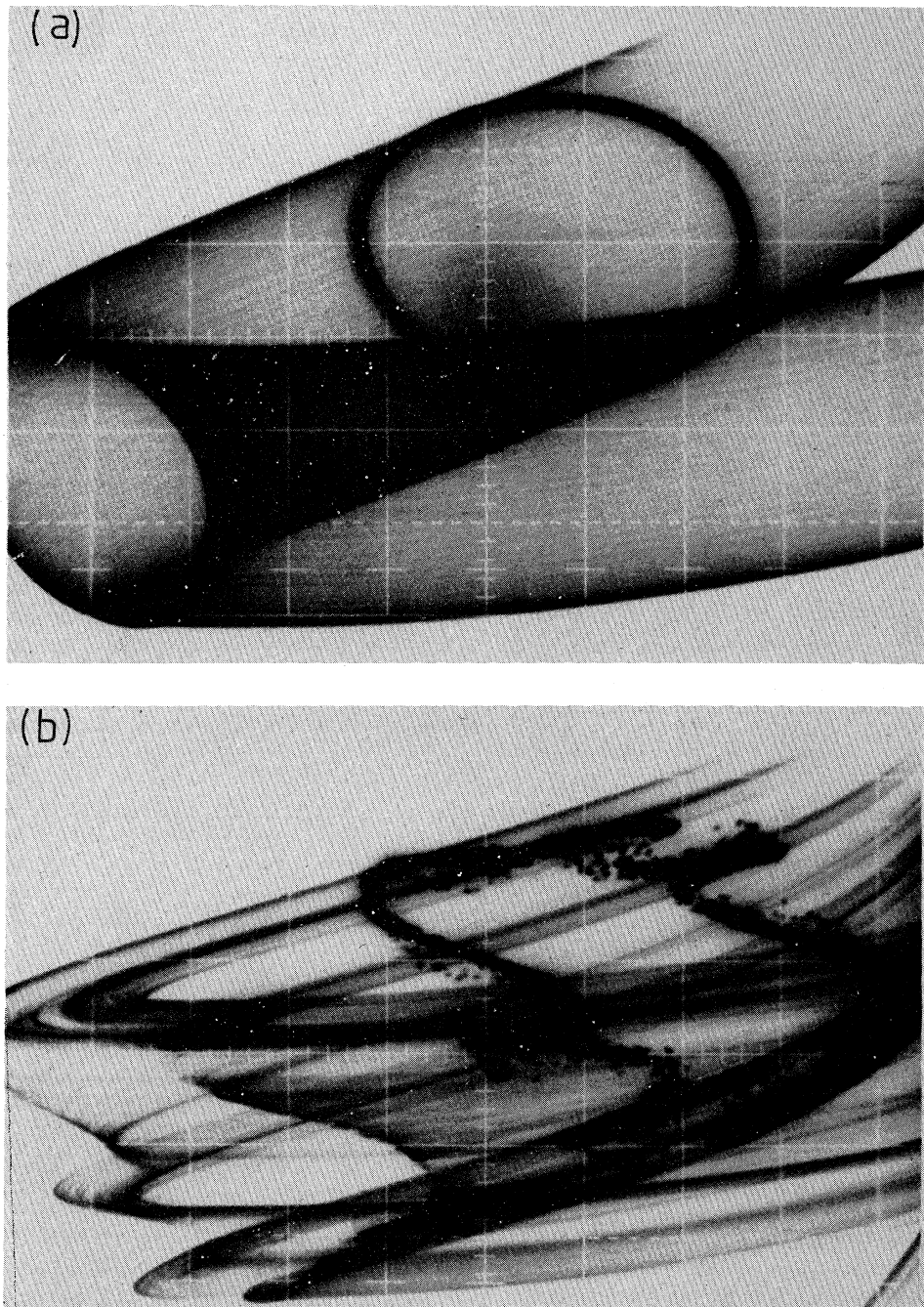


FIG. 31. (a) Phase portrait, $I_2(t)$ vs $V_1(t)$, for two resistively coupled junctions, showing piece of two-loop torus and strobed circular Poincaré section; $V_{os}=3.2$ V rms. (b) At $V_{os}=4.8$ V rms torus is broken up, the Poincaré section is the dark “rabbit”-like object. $L=100$ mH, $R_C=1200$ Ω , $f=27.1$ kHz, 1N4723 junction.

There is first a single loop which bifurcates to a double loop as the drive voltage is increased; then there occurs a Hopf bifurcation to a double-loop torus. The projection of one loop of this torus onto the (I_2, V_1) plane is shown in Fig. 31(a) for $V_{os}=3.2$ V rms; the dark circle is a Poincaré section strobed at $t=nT$. At $V_{os}=4.2$ V rms the torus has broken up: the Poincaré section, Fig. 31(b), resembles a "strange rabbit." We next show the details of the breakup of this circle, a simple graphic view of events on the road to chaos in this system (for the exact same system, Fig. 23 shows the bifurcation diagram, Fig. 34 the power spectra, and Fig. 29 the phase diagram). As V_{os} is increased, we see in the Poincaré sections of Fig. 32 (a) the invariant circle just after the Hopf bifurcation, (b) wrinkling of the circle, (c) more wrinkling, with small folds, (d) frequency locking, $f_1/f_2 = \frac{18}{4}$. In Fig. 33 we see (a) period doubling, (b) nine-band chaos, strange ("rabbit") attractor, (c) folding, (d) more folding, a "folded rug" attractor. There is another similar attractor corresponding to the lower branch of Fig. 23(a).

The models, Eqs. (12) and (15), yield computed Poincaré sections similar to those observed. We also point out the good correspondence between our data and sections computed for two coupled logistic maps. For example, the folded rug of Fig. 33(d) is visually quite similar to the attractor computed by Froyland (Ref. 25, Fig. 5, lower),

by Kaneko [Ref. 26, Fig. 2(f)], and by Hogg and Huberman [Ref. 28, Fig. 7(a)]. The rabbit of Fig. 33(b) is similar to Ref. 25, Fig. 5, upper. The general sequence, Figs. 32 and 33, is also qualitatively represented by Poincaré sections computed by Curry and Yorke³⁸ for a map of the plane. The sequence is perhaps even more similar to those computed by Kaneko³⁰ for a two-dimensional delayed logistic map.

Fractal dimension. Using the method described in Sec. II we measure a fractal dimension of the attractor under conditions similar to those for Fig. 33(d). For $R_C=1200$ Ω , $V_{os}=7.191$ V rms, $f_1=29.671$ kHz, we sampled $q=96000$ consecutive values of $I_1(t)$ by strobing asynchronously with reference to the drive period. This data yielded $d=2.23\pm 0.04$ in a plot similar to Fig. 22, with embedding dimension $D=6$. It is not yet clear if anything significant can be said about this value of d . If the two oscillators are very strongly coupled, one expects the temporal behavior of $I_1(t)$ to be representative of the whole system, operationally represented by $I_s(t) = I_1(t) + I_2(t)$, so that a measurement of dimension d_1 from the time series $I_1(t)$ should yield essentially the same value as d_s from $I_s(t)$. However, if the coupling is reduced to zero, we have complete localization and $I_1(t)$ and $I_2(t)$ have no temporal correlation; one then expects $d_s \approx 2d_1$. Similar ideas apply to a line of N identical os-

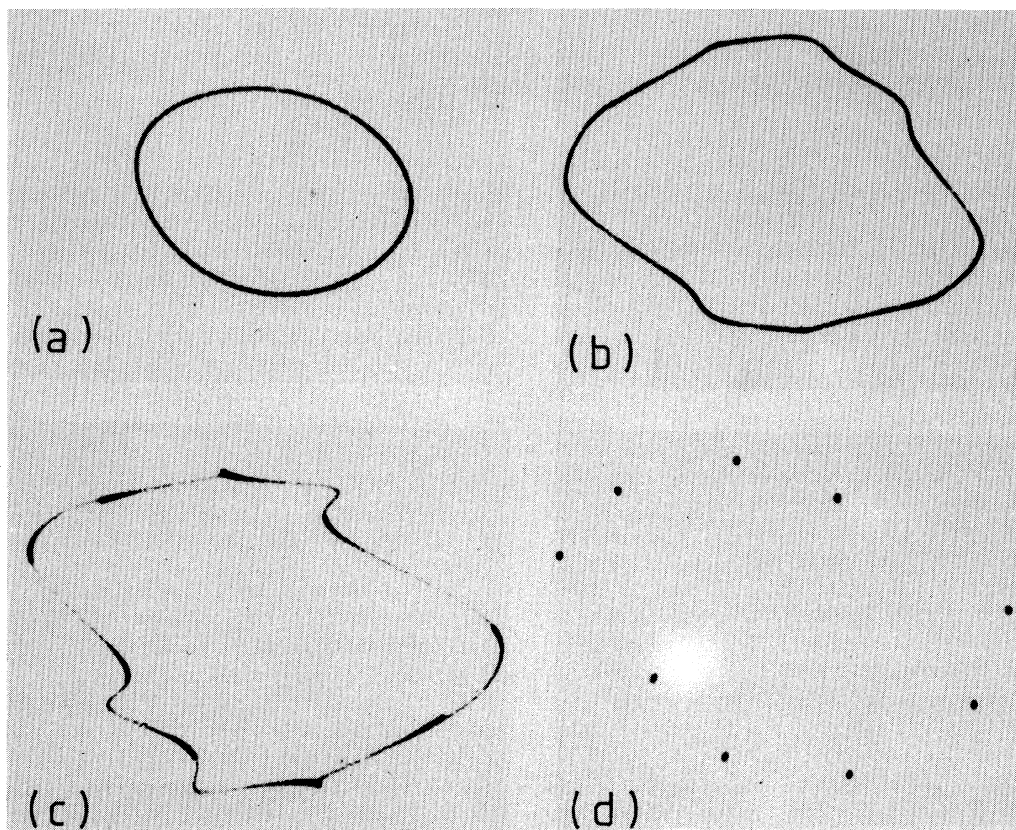


FIG. 32. Sequence of Poincaré sections, I_2 vs V_1 , for two resistively coupled junctions (Fig. 31) for increasing drive voltage V_{os} (V rms): (a) 3.165, smooth circle just after Hopf bifurcation; (b) 3.681, wrinkled circle; (c) 4.028, more wrinkled; (d) 4.190, entrainment (locking) at $f_1/f_2 = 18/4$.

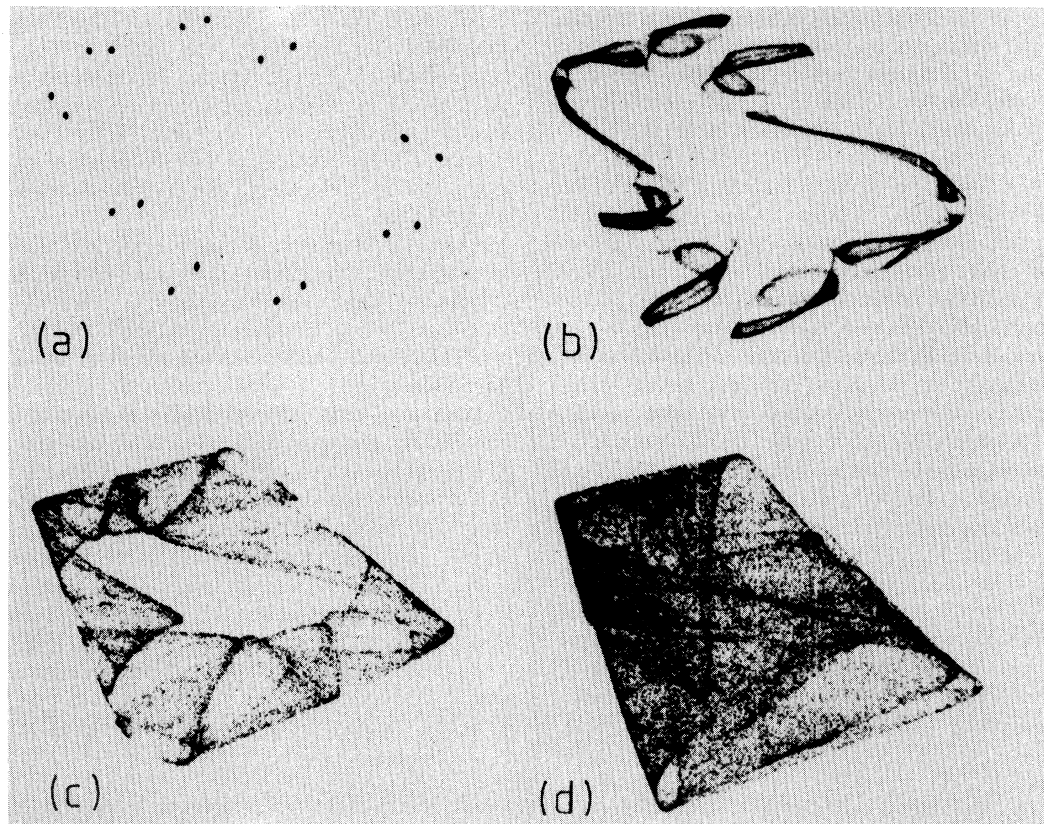


FIG. 33. Sequence of Poincaré sections, I_2 vs V_1 , continued from Fig. 32. (a) $V_{os}=4.409$, period doubling of locked state; (b) 4.882, strange rabbit attractor; (c) 5.132, folding; (d) 8.958, more folding.

cillators where some localization may occur even if the coupling is nonzero.³⁹

Power spectra. For each of the values of the drive voltage in the sequence of Figs. 32 and 33 we recorded the power spectrum, shown in Fig. 34. For $V_{os} < 3.1$ V rms the spectrum is a set of sharp lines at $f_1/2, f_1, 3f_1/2$, etc. The new frequency f_2 appears after the Hopf bifurcation in Fig. 34(a), together with the combination frequencies $f_1/2 - f_2, f_1/2 + f_2$ (not shown), etc., all given by $f_{nm} = nf_1/2 + mf_2$ with m, n positive and negative integers. In Fig. 34(f) the rabbit attractor has appeared and the spectrum has broadband character: onset of chaos, in this instance, by period doubling. In Fig. 34(h) the spectrum is very broadband with sharp peaks at $f_1/2$ and f_1 and their harmonics (not shown).

Oscillations of the torus. Figure 35 shows two Poincaré sections for increasing drive voltage following Hopf bifurcation just prior to locking at $P/Q=4/1$. The counter clockwise orbit rapidly approaches the upper right-hand corner, bends left, slows down, and develops damped transverse oscillations. The orbit lingers near points A and B , Fig. 35(b), which become stable fixed points. Similar-looking orbits have been computed for two coupled logistic maps [see Ref. 28, Fig. 6(a)]. Insight into the details for a similar case is given by Kaneko,³⁰ who studied the oscillations for a two-dimensional delayed logistic

map. He attributes the effect to damped oscillation of an unstable manifold of a periodic saddle. Figure 36 is a schematic showing two stable fixed points with manifolds M_{sa} and M_{sp} along the amplitude and phase directions, respectively, and two (unstable) saddle points with manifolds M_{ua} and M_{up} . If M_{up} crosses M_{sp} once, it must cross an infinite number of times, hence the oscillations of M_{up} . The damping is determined by the eigenvalue λ_{sa} of the Jacobian matrix, which is close to -1 near the bifurcation point, where the oscillations have maximum amplitude. This model gives a good qualitative explanation of our observations. It is related to heteroclinic crossings in area-preserving maps, but the oscillations in our case are damped.

Crises of the attractor.⁸ Another example of characteristic behavior of coupled oscillators is shown in Fig. 37. After period doubling and a Hopf bifurcation, the system is entrained at $P/Q=14/3$, Fig. 37(a); by increasing the drive voltage there is another Hopf bifurcation to 14 "island" attractors; the seven upper islands are shown in Fig. 37(b). As the drive voltage is further increased, these begin to break up, and a crisis ensues: a cyclic collision of the seven attractors with the boundaries that separate the basins of attraction, resulting in a sudden merging into one attractor, Fig. 37(c). This behavior is expected theoretically and has been noted in computations for two

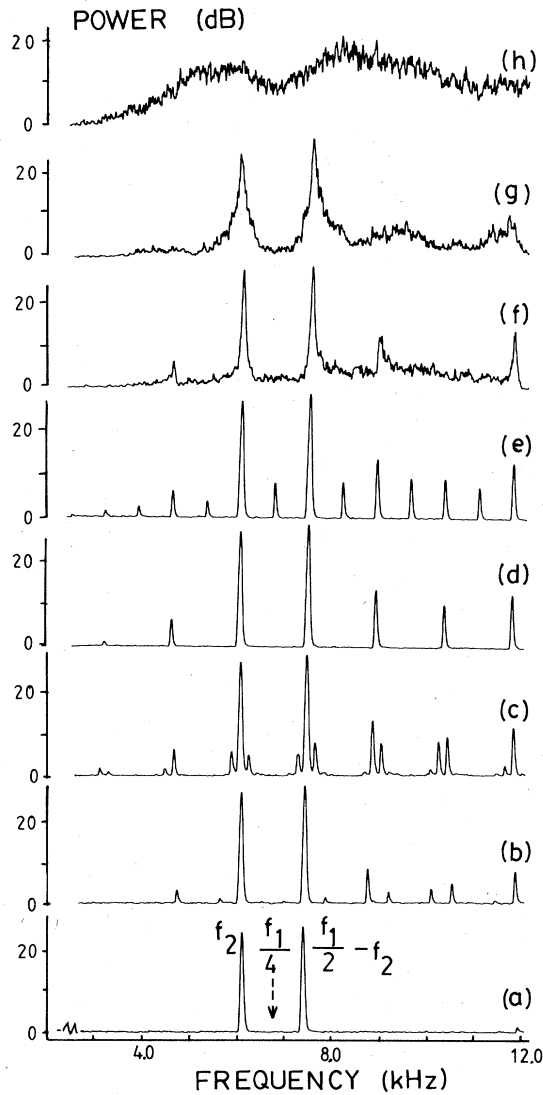


FIG. 34. Power spectra, P in dB vs frequency for two resistively coupled junctions, for same sequences of drive voltage as in Figs. 32 and 33, V_{os} (V rms): (a) 3.165, (b) 3.681, (c) 4.028, (d) 4.190, (e) 4.409, (f) 4.882, (g) 5.132, (h) 8.958.

coupled logistic maps (Ref. 29, Fig. 5; Ref. 25, Fig. 6).

Symmetry. For two resistively coupled junctions with very weak coupling ($R_C=83 \Omega$) Fig. 38 shows that the two junction waveforms $V_1(t)$ and $V_2(t)$ are in time phase (a) before and (b) after a period-doubling bifurcation, leading to chaos, (c). No Hopf bifurcation is observed. When the coupling is slightly increased ($R_C=107 \Omega$), the waveforms are initially in time phase, Fig. 38(d), then become out of phase just at the period-doubling bifurcation, (e); there follows a Hopf bifurcation, (f); chaos is reached at much higher drive voltages (not shown). For two line-coupled junctions, where the coupling cannot be made very weak, Fig. 38(g) shows that even for low drive voltages the waveforms are out of phase, and remain so as a

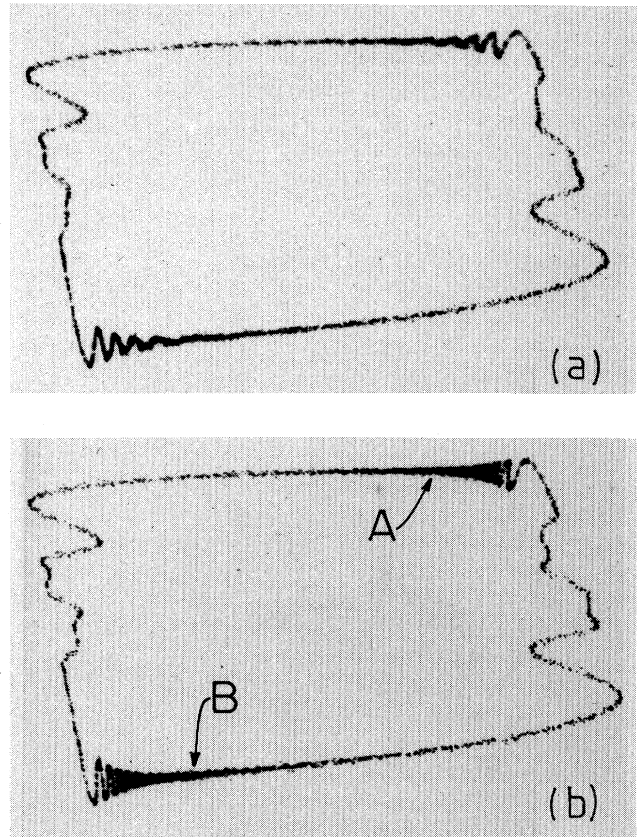


FIG. 35. Poincaré section, I_2 vs V_1 , for two resistively coupled junctions showing oscillation of the torus near period-4 locking. (a) $V_{os}=1.976$ V rms, (b) $V_{os}=2.003$. At $V_{os}=2.045$ points A and B become stable fixed points. $L=100$ mH, $R_C=510 \Omega$, $f=27.164$ kHz, 1N4723 junction.

Hopf bifurcation [Fig. 38(h)] is reached; no period doubling occurs. These two types of symmetry, in phase and out of phase, correspond crudely to the two modes of two line-coupled oscillators. Generally, we observe that a Hopf bifurcation can occur only from an out-of-phase state. This is consistent with Kaneko's phase diagram²⁶ for two coupled logistic maps; see also Refs. 25 and 28 for a similar treatment of the effects of symmetry.

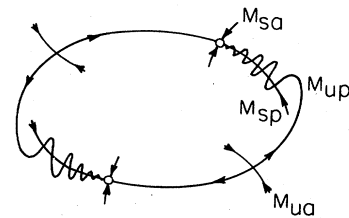


FIG. 36. Two periodic stable points (\circ) and manifolds M_{sa}, M_{sp} ; two unstable saddle points (\times) and manifolds M_{ua}, M_{up} . Damped radial oscillations occur where M_{up} intersects M_{sp} [after Ref. 30 (1984), Figs. 2 and 4].

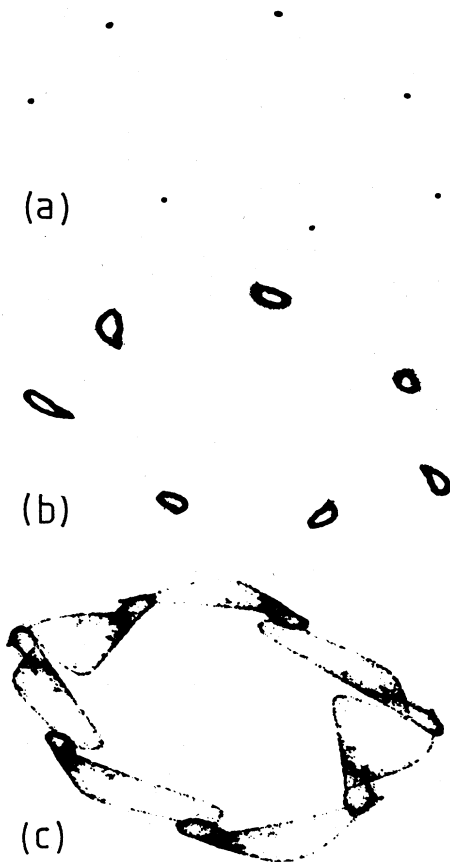


FIG. 37. Poincaré sections, I_2 vs V_1 , for two resistively coupled junctions showing (a) frequency locking ($P/Q=14/3$) at $V_{os}=6.152$; there is a second set of seven dots corresponding to the lower branch of the attractor (not shown); (b) $V_{os}=6.298$, second Hopf bifurcation; (c) $V_{os}=6.359$, cyclic crisis. $L=100$ mH, $R_C=1200$ Ω , $f=24.46$ kHz, 1N4723 junction.

C. Line coupling: Experiments and interpretation

Figure 39 is a bifurcation diagram observed for two line-coupled resonators, connected as explained in the caption of Fig. 1. This is analogous to a nonlinear transmission line with inductors in series and p - n junctions in shunt.⁴⁰ This system displayed first a Hopf bifurcation, then locking, period doubling, chaos, locking, etc., in a quite complex diagram. For comparison, Fig. 40 is a bifurcation diagram computed from the map model, Eq. (15) with $\gamma=0.8$, $b=0.95$, and $-C'=C=0.5$. It shows an overall resemblance to the data including the first Hopf bifurcation and the bifurcation to period 3 and period 6.

Figure 41 shows the breakup of the circle in the (I_2, V_2) Poincaré section as the drive voltage is increased. Figure 42 shows corresponding sections computed from the map model, Eq. (15), with $\gamma=0.8$, $b=0.95$, and $-C'=C=0.5$, $J=0.1$. The overall agreement is good if one compares the structural features.

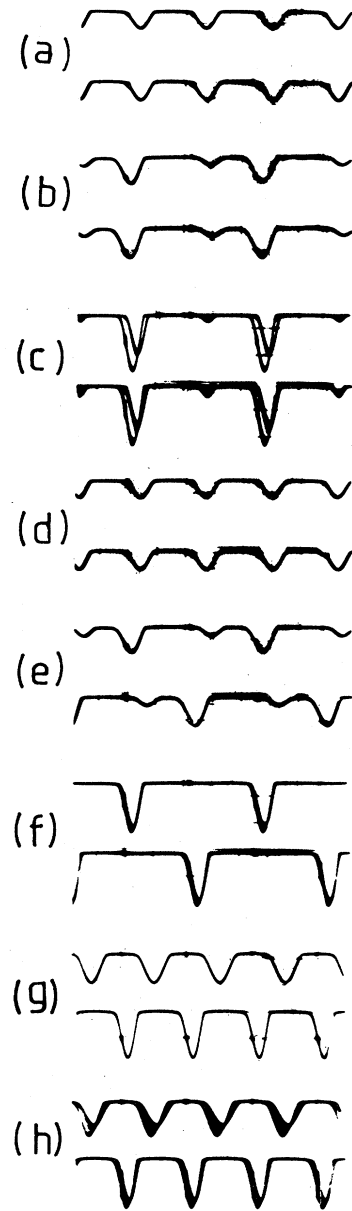


FIG. 38. Junction voltage waveforms, $V_1(t)$ and $V_2(t)$, for two coupled junctions for $R_C=83$ Ω : (a) $V_{os}=0.513$ V rms; (b) $V_{os}=0.645$, period doubling; (c) $V_{os}=1.913$, onset of chaos. For $R_C=106$ Ω : (d) $V_{os}=0.519$; (e) $V_{os}=0.645$, jump to out of phase and period doubling; (f) $V_{os}=1.641$, Hopf bifurcation from out-of-phase state. For line coupling, (g) $V_{os}=1.134$; (h) $V_{os}=1.158$, Hopf bifurcation. $L=100$ mH, $f=20$ kHz.

V. COUPLED OSCILLATORS WITH $N > 2$

For $N=4$ line-coupled junction resonators we observed the power spectra of Fig. 43 at increasing drive voltage at frequency f_1 . In Fig. 43(a) the system has made a Hopf bifurcation to a second frequency f_2 . In Fig. 43(b) a second bifurcation to a third frequency f_3 has occurred. In Fig. 43(c) the intensity of f_3 is more fully developed.

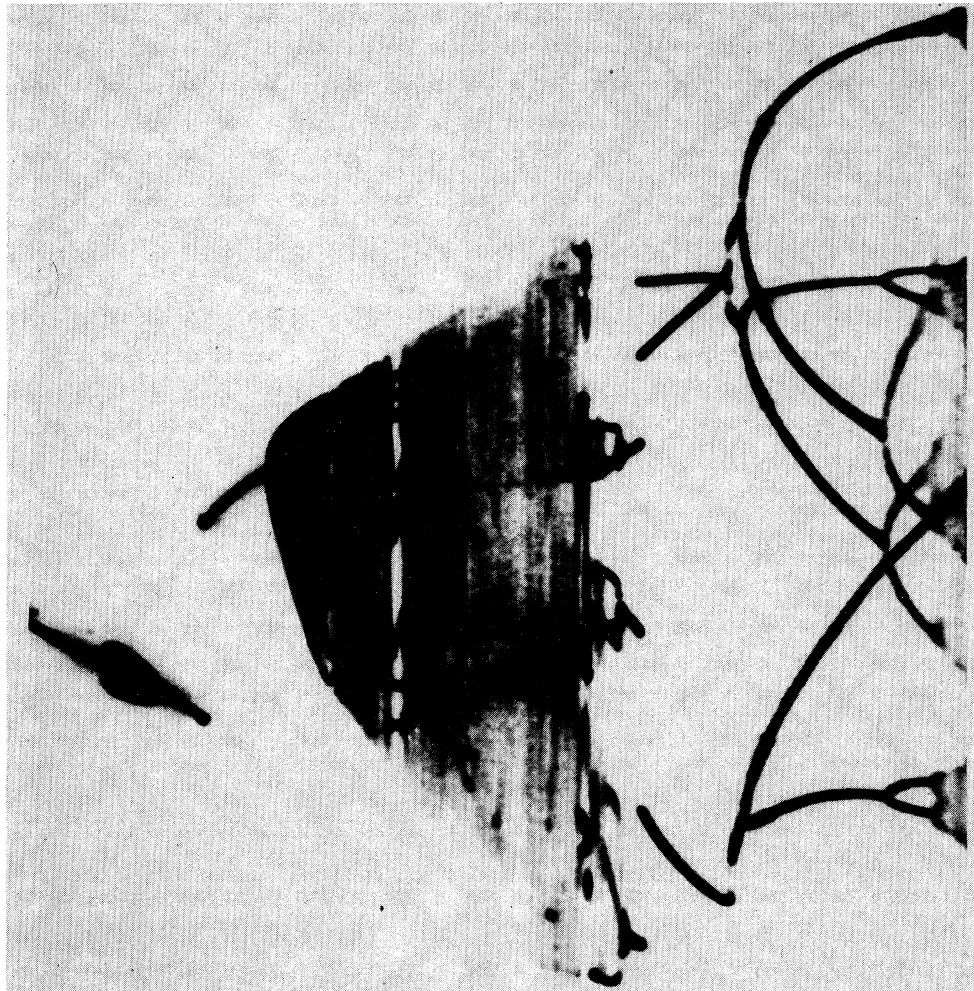


FIG. 39. Observed bifurcation diagram $\langle I_n \rangle$ vs V_{os} for two identical line-coupled resonators showing Hopf bifurcation and frequency locking. $L = 8.2$ mH, $R_0 = 70$ Ω , $f = 90$ kHz, 1N4723 junction.

All lines in this quasiperiodic spectrum are fit by the expression for the combination frequency

$$f = m_1 f_1 + m_2 f_2 + \cdots + m_i f_i \quad (18)$$

with the set of integers (m_1, \dots, m_i) shown in the figure. Figure 43(a) is fit by two frequencies, and (b)–(d) by three frequencies: $f_1 = 167$ kHz, $f_2 \cong 63.6$ kHz, $f_3 \cong 11.53$ kHz. f_1 is set by the drive oscillator, whereas f_2 and f_3 are determined by the system dynamics and depend on the drive voltage, but this dependence has not been measured. We believe that if any two frequencies f_i and f_j are locked, then the locking ratio f_i/f_j must have integers larger than at least 30 since with our apparatus we could have observed such ratios. Within this error we believe that the three frequencies are incommensurate. We note that as the drive voltage is increased, the spectral intensity at f_3 and its combination frequencies is increased, e.g., the line $f_1 - f_3$ in Fig. 43(c). Figure 43(d) shows onset of chaos: there is the beginning of a broadband line centered

at $f_1 - f_3$. If there is a fourth frequency, its intensity must be at least 10 dB below that of f_3 .

For $N = 12$ junction resonators with line coupling, the observed power spectra are shown in Fig. 44, for increasing values of drive voltage. As in all line-coupled systems there is a first Hopf bifurcation to a second frequency f_2 , then to a third frequency f_3 , etc. All spectral lines in Fig. 44 can be fit by Eq. (18) extended to four frequencies. Figure 44(a)–(d) require 2, 2, 3, and 4 frequencies, respectively. This conclusion is supported by the direct observation of the following Poincaré sections: Fig. 44(a), a single loop (a section of a 2-torus); Fig. 44(b), a complicated loop (but still a section of a 2-torus); Fig. 44(c), a complicated 2-torus (a section of a 3-torus); Fig. 44(d), an object suggestive of a 2D projection of a 3-torus (itself a section of a 4-torus). Chaos is just beginning to set in for Fig. 44(d). On the whole it was difficult to experimentally find the parameter values (V_{os}, f_1) at which quasiperiodicity with four frequencies was observed.

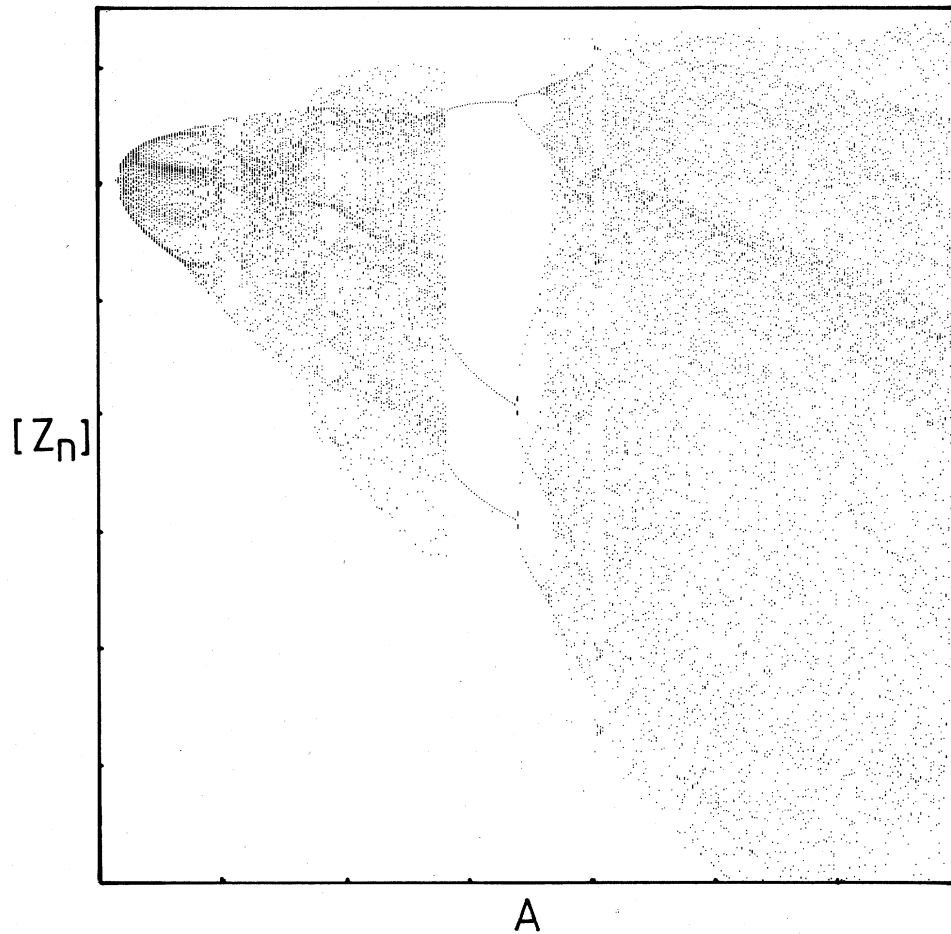


FIG. 40. Bifurcation diagram $[Z_n]$ vs A for line-coupled iterative map model, Eq. (15), with $\gamma=0.8$, $b=0.95$, $-C'=C=0.5$, $J=0.1$.

VI. SUMMARY AND CONCLUSIONS

A driven p - n junction resonator is highly nonlinear with an asymmetric weak-strong restoring force, owing to charge storage in forward injection. The system displays a period-doubling cascade to chaos, which is part of a larger period-adding sequence in which the resonator is entrained to successive subharmonics of the drive frequency. To model the effects of dissipation, attractors are computed for various values of a in an exponential force model, Eq. (9); the results, Fig. 5, show a marked dependence of the fractal dimension on a . Measured bifurcation diagrams are reasonably similar to those computed from a three-dimensional ODE model [Eq. (3)] and a two-dimensional iterative map model [Eq. (11)] with a form chosen to represent the junction resonator characteristics. The measured phase diagram in parameter space (drive voltage, drive frequency) is similar to that computed from Eq. (3). At low drive voltage the observed return map is similar to that computed from Hénon's map, Eq. (7), with contraction ratio $J \approx -0.1$. Poincaré sections show self-similarity and fractal structure; a fractal dimension $d = 2.04 \pm 0.03$ is measured for the one-band chaotic

attractor just before the period-3 window for a particular set of system parameters.

For two resistively coupled junction resonators we find two-frequency quasiperiodicity. As the drive voltage is increased we observe: period $1 \rightarrow 2$ doubling, Hopf bifurcation to a second incommensurate frequency, entrainment, additional Hopf bifurcations and/or period doubling, chaos. Bifurcation diagrams are compared to those computed from a coupled ODE model, Eq. (12); and also to an iterative map model, fashioned from coupling two two-dimensional maps, Eq. (15). Qualitative agreement is found; two coupled logistic maps are also found to be a reasonable model. The phase diagram in parameter space (drive voltage, drive frequency) is found to display entrainment horns emanating from the Hopf bifurcation boundary, with period doubling within a horn. The major boundaries in the phase diagram can be understood by computations using Eq. (12). The breakup of the torus is observed in detail, simultaneously in Poincaré sections and in power spectra. The strange attractor is found to be quite similar to that from maps of the plane. A fractal dimension $d = 2.23 \pm 0.04$ was measured for a "fully folded" strange attractor. Other generic behavior reported in-

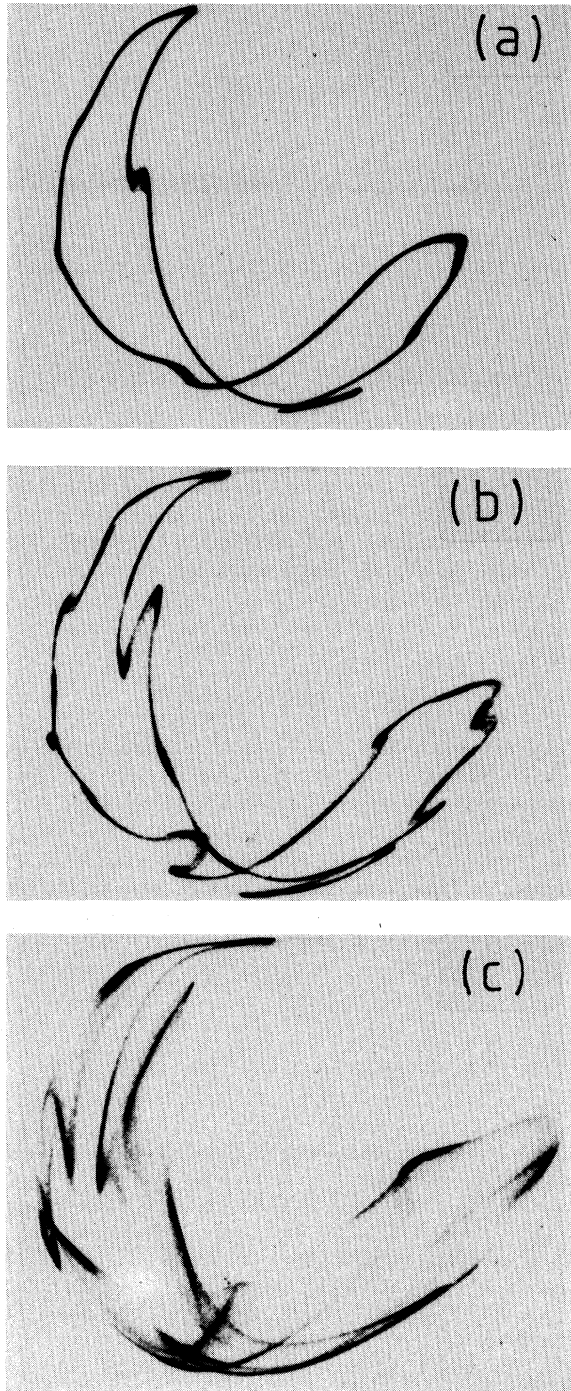


FIG. 41. Observed Poincaré sections, V_2 vs I_2 , for two line-coupled junctions for increased drive voltage, from (a) to (c), showing breakup of the torus; system same as in Fig. 39.

cludes oscillators of the torus, cyclic crises of the attractor; and effects of coupling on the symmetry.

For two line-coupled junction resonators we find first a Hopf bifurcation as the drive voltage is increased in contrast to the resistively coupled case. This is found to be in

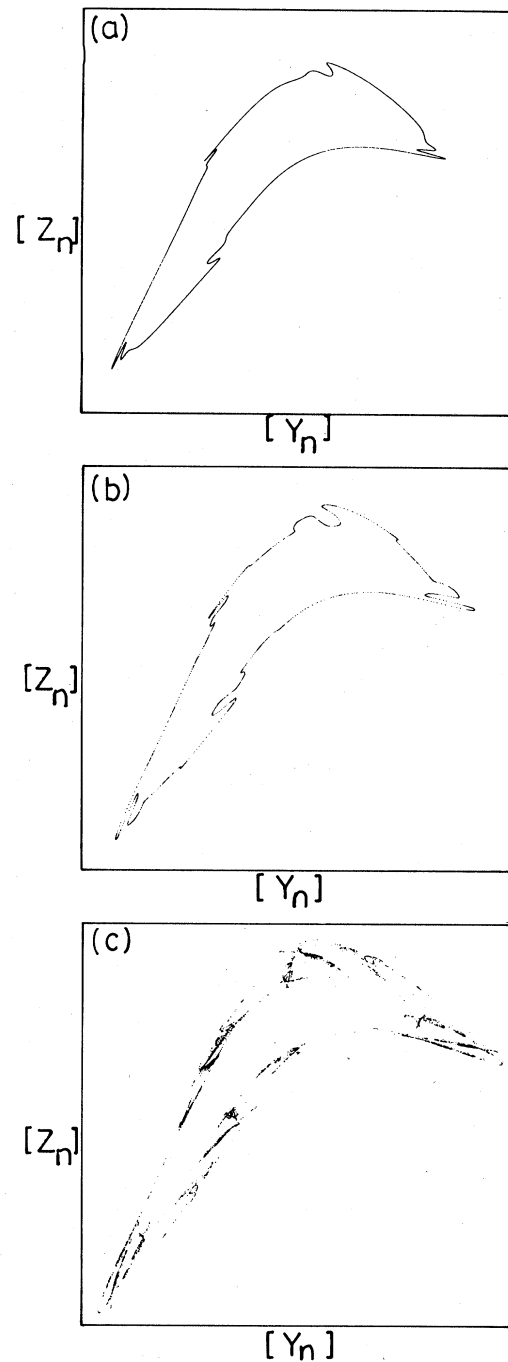


FIG. 42. Computed Poincaré sections of $[Z_n]$ vs $[Y_n]$ computed from map model, Eq. (15), with $\gamma=0.8$, $b=0.95$, $-C'=C=0.5$, $J=0.1$. (a) $A=2.25$, (b) $A=2.29$, (c) $A=2.357$.

agreement with the model, Eq. (15), which also explains reasonably the Poincaré sections.

For a line of $N=4$ coupled resonators we find quite complex behavior in bifurcation diagrams; almost any sequence of patterns can occur. Power spectra are fit to

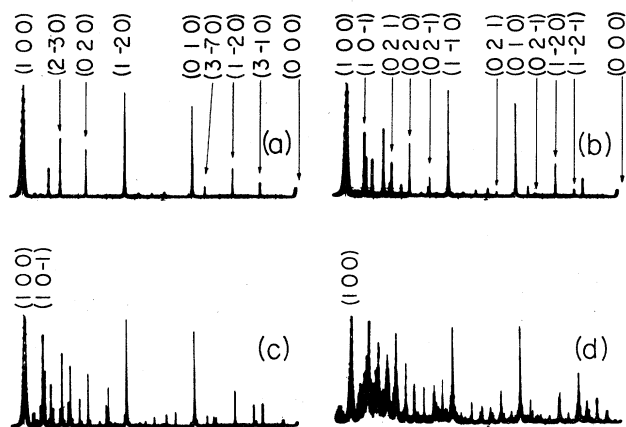


FIG. 43. Quasiperiodic power spectrum (relative dB vertical) observed for $N=4$ identical line-coupled junctions for increased drive voltage, from (a) to (d), with integers (m_1, m_2, m_3) in Eq. (16) which classify the spectrum lines. This system is quasiperiodic with three incommensurate frequencies. $L=8.2$ mH, $R=70$ Ω , drive frequency $f_1=167$ kHz, 1N4723 junctions.

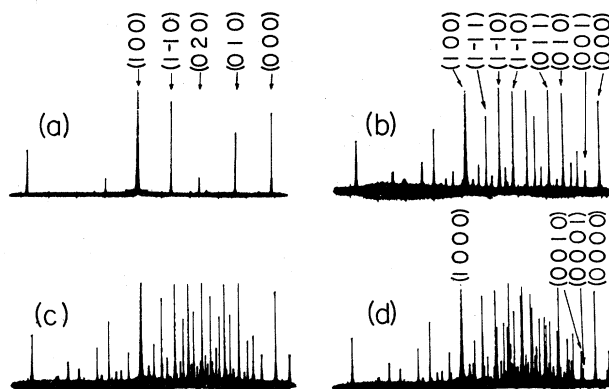


FIG. 44. Quasiperiodic power spectrum (relative dB vertical) observed for $N=12$ identical line-coupled junctions for increased drive voltage, from (a) to (d). The spectrum lines in (a) and (b) can be fit by Eq. (16) with (m_1, m_2, m_3) shown. (c) requires three frequencies and (d) requires four frequencies. $L=8.2$ mH, $R=70$ Ω , drive frequency is $f_1=220$ kHz, 1N4723 junction.

three-frequency quasiperiodicity. For $N=12$ resonators we find four-frequency quasiperiodicity. No attempts were made to model the detailed behavior for these cases.

In conclusion, we find that the chaotic dynamics of $N=1$ and $N=2$ coupled $p-n$ junction resonators can be reasonably understood by tractable models. The driven $p-n$ junction is a simple but very useful physical system for further study of quasiperiodicity in high-dimensional systems, e.g., the question of localization. Such studies are now in progress.

ACKNOWLEDGMENTS

We thank Jose Perez for his help on some aspects of this work, Glenn Held for collaboration on the fractal measurements, and James Crutchfield, Paul Bryant, and James Testa for helpful discussions. One of us (C.D.J.) thanks the Miller Institute for Basic Research in Science for support. This work was supported by the Director, Office of Energy Research, Office of Basic Energy Sciences, Materials Sciences Division of the U.S. Department of Energy under Contract No. DE-AC03-76SF00098.

*Present address: Department of Physics, Harvard University, Cambridge, MA 02138.

¹P. S. Linsay, Phys. Rev. Lett. **47**, 1349 (1981).

²M. J. Feigenbaum, J. Stat. Phys. **19**, 25 (1978).

³J. Testa, J. Perez, and C. Jeffries, Phys. Rev. Lett. **48**, 714 (1982); J. Perez, Thesis, 1983, University of California, Berkeley (Lawrence Berkeley Laboratory Report No. LBL-16898).

⁴R. W. Rollins and E. R. Hunt, Phys. Rev. Lett. **49**, 1295 (1982); E. R. Hunt and R. W. Rollins, Phys. Rev. A **29**, 1000 (1984); H. Ikezi, J. S. deGrassie, and T. H. Jensen, *ibid.* **28**, 1207 (1983); S. D. Brorson, D. Dewey, and P. S. Linsay, *ibid.* **28**, 1201 (1983); J. Perez and C. Jeffries, Phys. Lett. **92A**, 82 (1982); P. Klinker, W. Meyer-Ilse, and W. Lauterborn, *ibid.* **101A**, 371 (1984).

⁵C. Jeffries and J. Perez, Phys. Rev. A **26**, 2117 (1982).

⁶J. Perez and C. Jeffries, Phys. Rev. B **26**, 3460 (1982).

⁷C. Jeffries and K. Wiesenfeld, Phys. Rev. A **31**, 1077 (1985).

⁸C. Grebogi, E. Ott, and J. A. Yorke, Phys. Rev. Lett. **48**, 1507 (1982).

⁹C. Jeffries and J. Perez, Phys. Rev. A **27**, 601 (1983); R. W. Rollins and E. R. Hunt, *ibid.* **29**, 3327 (1984).

¹⁰R. Van Buskirk, Thesis, 1984, University of California, Berkeley

(Lawrence Berkeley Laboratory Report No. LBL-17868).

¹¹C. D. Jeffries, Phys. Scr. (to be published).

¹²For reviews of theory see J.-P. Eckmann, Rev. Mod. Phys. **53**, 643 (1981); E. Ott, *ibid.* **53**, 655 (1981); J. Guckenheimer and P. Holmes, *Nonlinear Oscillators, Dynamical Systems and Bifurcations of Vector Fields* (Springer, New York, 1983).

¹³See, e.g., S. Wang, *Solid State Electronics* (McGraw-Hill, New York, 1966), Chap. 6.

¹⁴N. H. Packard, J. P. Crutchfield, J. D. Farmer, and R. S. Shaw, Phys. Rev. Lett. **45**, 712 (1980).

¹⁵S. D. Conte and C. de Boor, *Elementary Numerical Analysis* (McGraw-Hill, New York, 1980).

¹⁶See, e.g., J. Swift and K. Wiesenfeld, Phys. Rev. Lett. **52**, 705 (1984).

¹⁷See, e.g., D. W. Jordan and P. Smith, *Nonlinear Ordinary Differential Equations* (Clarendon, Oxford, 1977), Chap. 7.

¹⁸See, e.g., J. Guckenheimer and P. Holmes, in Ref. 12, p. 149.

¹⁹J. L. Kaplan and J. A. Yorke, in *Functional Differential Equations and Approximations of Fixed Points*, Vol. 730 of *Lecture Notes in Math*, edited by Heinz-Otto Peitten and Heinz-Otto Walter, (Springer, New York, 1979) p. 228.

²⁰See, e.g., J. D. Farmer, E. Ott, and J. A. Yorke, *Physica* **7D**,

- 153 (1983); P. Grassberger and I. Procaccia, *Phys. Rev. Lett.* **50**, 346 (1983).
- ²¹Although an oscillator has only two dynamical variables, the driving term introduces a third variable, the phase of the driver.
- ²²We acknowledge with thanks the collaboration of G. Held in these experiments.
- ²³The experimental procedure follows ideas put forth by P. Grassberger and I. Procaccia, in Ref. 20; A. Brandstätter *et al.*, *Phys. Rev. Lett.* **51**, 1442 (1983); A. Ben-Mizrachi, I. Procaccia, and P. Grassberger, *Phys. Rev. A* **29**, 975 (1984).
- ²⁴D. Ruelle and F. Takens, *Commun. Math. Phys.* **20**, 167 (1971).
- ²⁵J. Froyland, *Physica* **8D**, 423 (1983).
- ²⁶K. Kaneko, *Prog. Theor. Phys.* **69**, 1427 (1983).
- ²⁷J.-M. Yuan, M. Tung, D. H. Feng, and L. M. Narducci, *Phys. Rev. A* **28**, 1662 (1983).
- ²⁸T. Hogg and B. A. Huberman, *Phys. Rev. A* **29**, 274 (1984).
- ²⁹Y. Gu *et al.*, *Phys. Rev. Lett.* **52**, 701 (1984).
- ³⁰K. Kaneko, Thesis, 1983, University of Tokyo; see also K. Kaneko, *Prog. Theor. Phys.* **72**, 202 (1984).
- ³¹S. J. Shenker, *Physica* **5D**, 405 (1982); M. J. Feigenbaum, L. P. Kadanoff, and S. J. Shenker, *ibid.* **5D**, 370 (1982); S. Ostlund, D. Rand, J. Sethna, and E. Siggia, *ibid.* **8D**, 303 (1983).
- ³²M. H. Jensen, P. Bak, and T. Bohr, *Phys. Rev. Lett.* **50**, 1637 (1983); (unpublished).
- ³³V. I. Arnold, *Trans. Am. Math. Soc.*, 2nd Ser. **46**, 213 (1965).
- ³⁴L. Glass and R. Perez, *Phys. Rev. Lett.* **48**, 1772 (1982); M. Schell, S. Fraser, and R. Kapral, *Phys. Rev. A* **28**, 373 (1983).
- ³⁵Similar qualitative expressions have been voiced. S. Ciliberto and J. Gollub, *Phys. Rev. Lett.* **52**, 922 (1984): “. . . pattern competition leads to chaos;” and M. H. Jensen, P. Bak, and T. Bohr, in Ref. 32, “. . . chaos is a frustrated response. . . .”
- ³⁶P. Bryant and C. Jeffries, *Phys. Rev. Lett.* **53**, 250 (1984).
- ³⁷P. Bryant and C. Jeffries, Lawrence Berkeley Laboratory Report No. LBL-16949 (unpublished).
- ³⁸J. H. Curry and J. A. Yorke, *Lect. Notes Math.* **688**, 48 (1978).
- ³⁹See, e.g., R. W. Walden, P. Kolodner, A. Passner, and C. M. Surko, *Phys. Rev. Lett.* **53**, 242 (1984).
- ⁴⁰For early experiments on similar nonlinear transmission lines operated in the nonchaotic regime, see R. Hirota and K. Suzuki, *J. Phys. Soc. Jpn.* **28**, 1366 (1970), *Proc. IEEE* **61**, 1483 (1973).

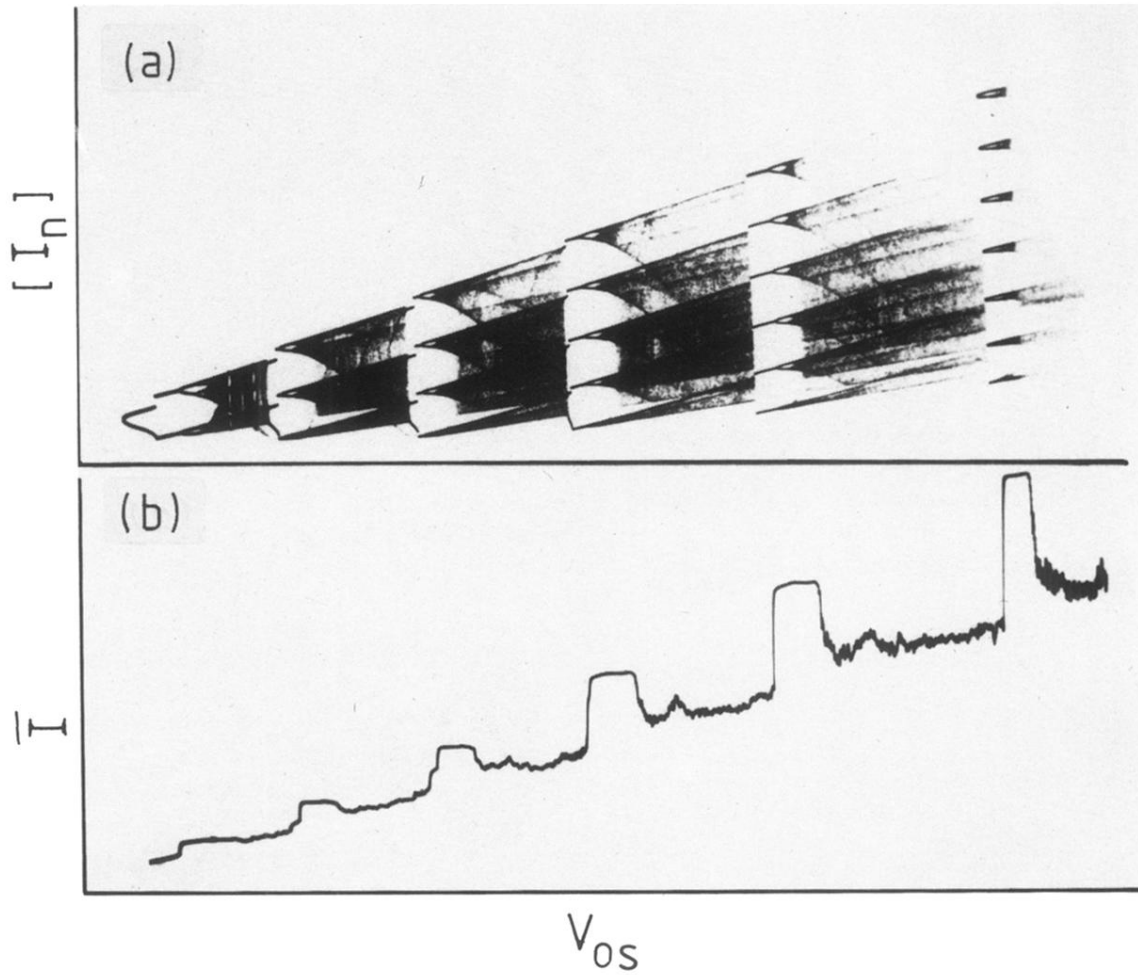


FIG. 10. (a) Bifurcation diagram $[I_n]$ vs drive voltage V_{os} (arbitrary units) for p - n junction showing period doubling and period adding (frequency locking). (b) Average junction current I vs V_{os} , showing peaks at locked regions. $f=28$ kHz, $L=10$ mH, $R=8$ Ω , 300 A p - n junction.

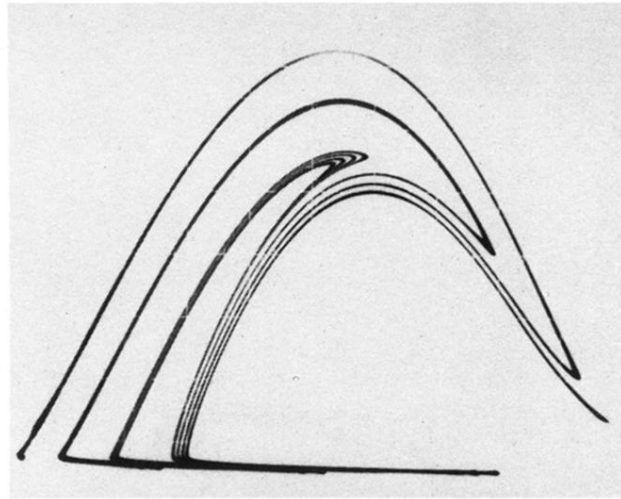


FIG. 15. Poincaré section, I vs \dot{I} , showing self-similarity and fractal structure. $L = 10$ mH, $f = 76$ kHz, $R = 43 \Omega$, 1N4721 junction.

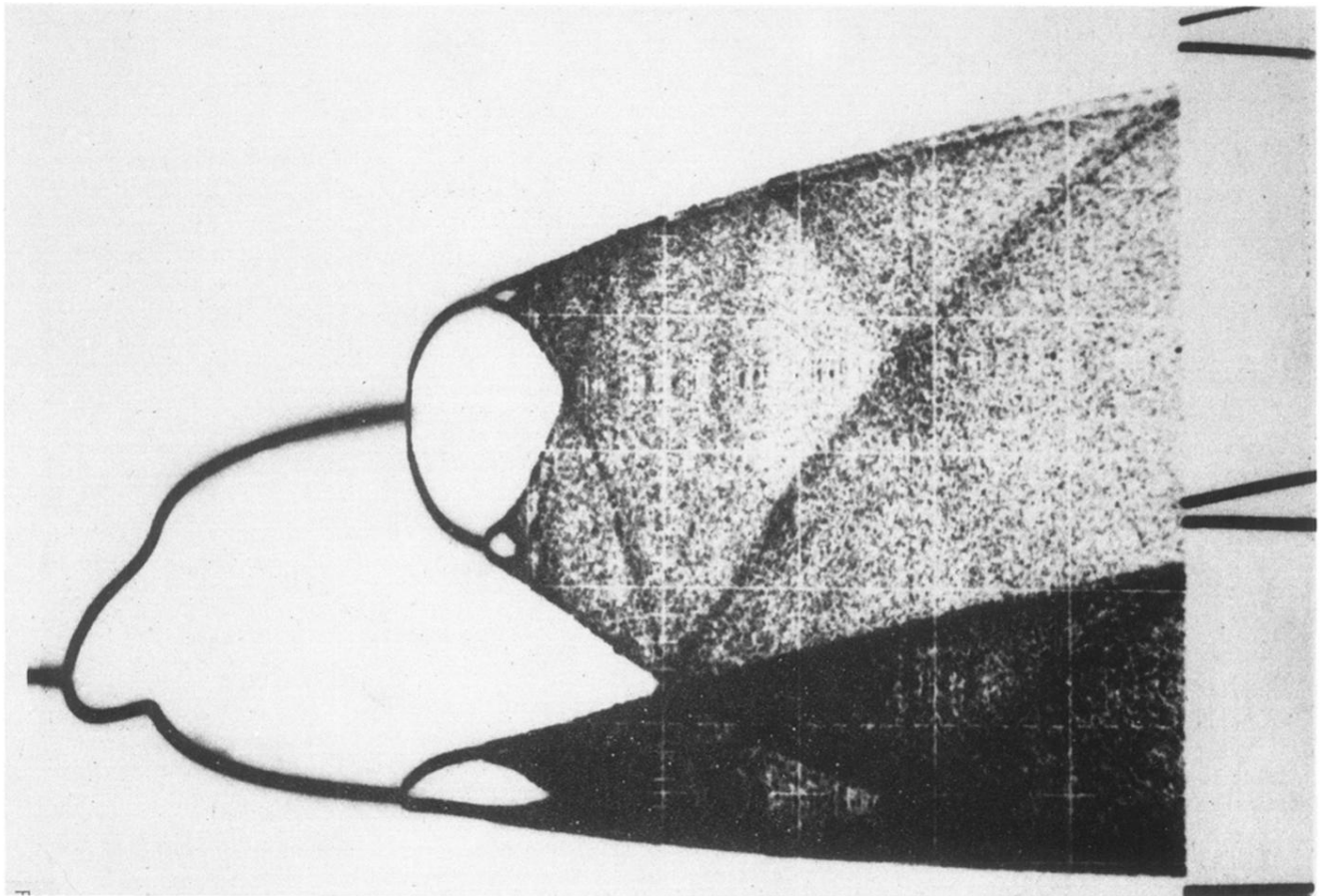


FIG. 17. Measured bifurcation diagram, $[I_n]$ vs V_{os} (horizontal, arbitrary units) for driven junction. $L = 100$ mH, $R = 53 \Omega$, $f = 20.3$ kHz, 1N4723 junction.

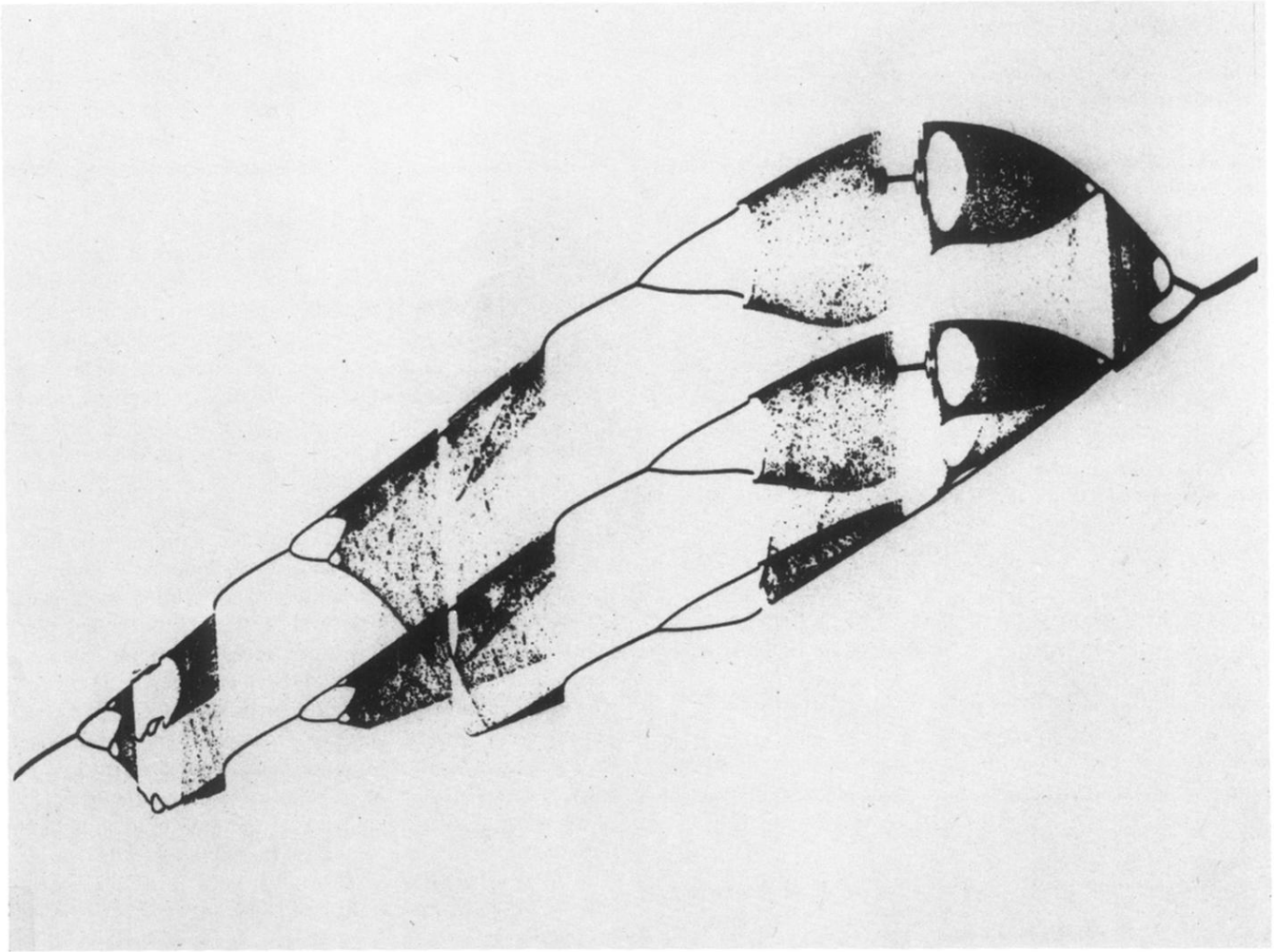


FIG. 20. Observed bifurcation diagram $[I_n]$ vs V_{os} (horizontal, arbitrary units) for driven junction, $f = 11.79$ kHz, $L = 10$ mH, $R = 8 \Omega$, 300 A junction.

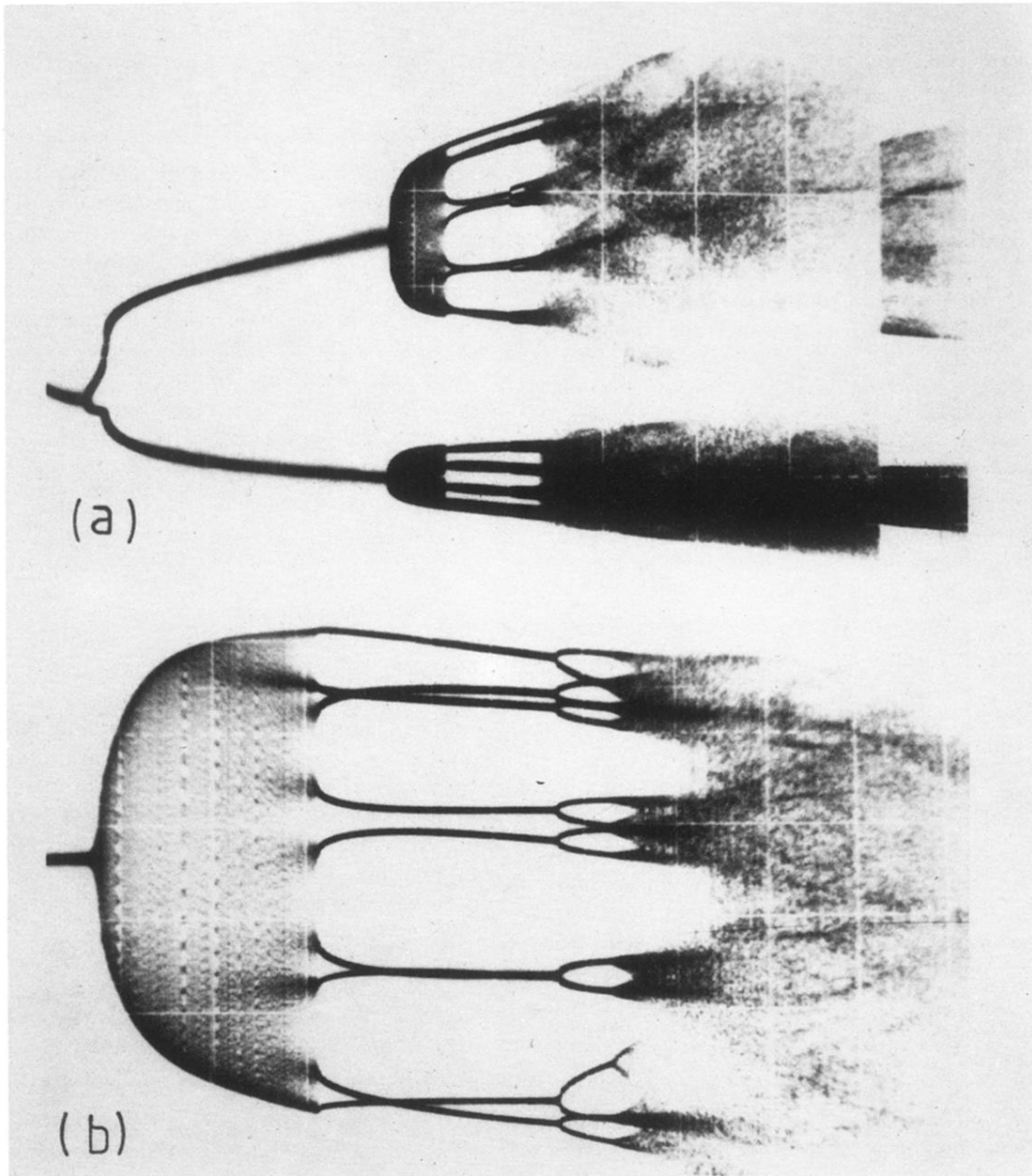


FIG. 23. (a) Bifurcation diagram $[I_n]$ vs V_{os} for two identical resistively coupled junctions, showing period doubling, Hopf bifurcations, and chaos. (b) Enlarged bifurcation diagram $[V_n]$ vs V_{os} of upper center section of (a), showing Hopf bifurcation, entrainment, doubling, chaos. $L = 100$ mH, $R_C = 1200$ Ω , $f = 27.127$ kHz, 1N4723 junction.

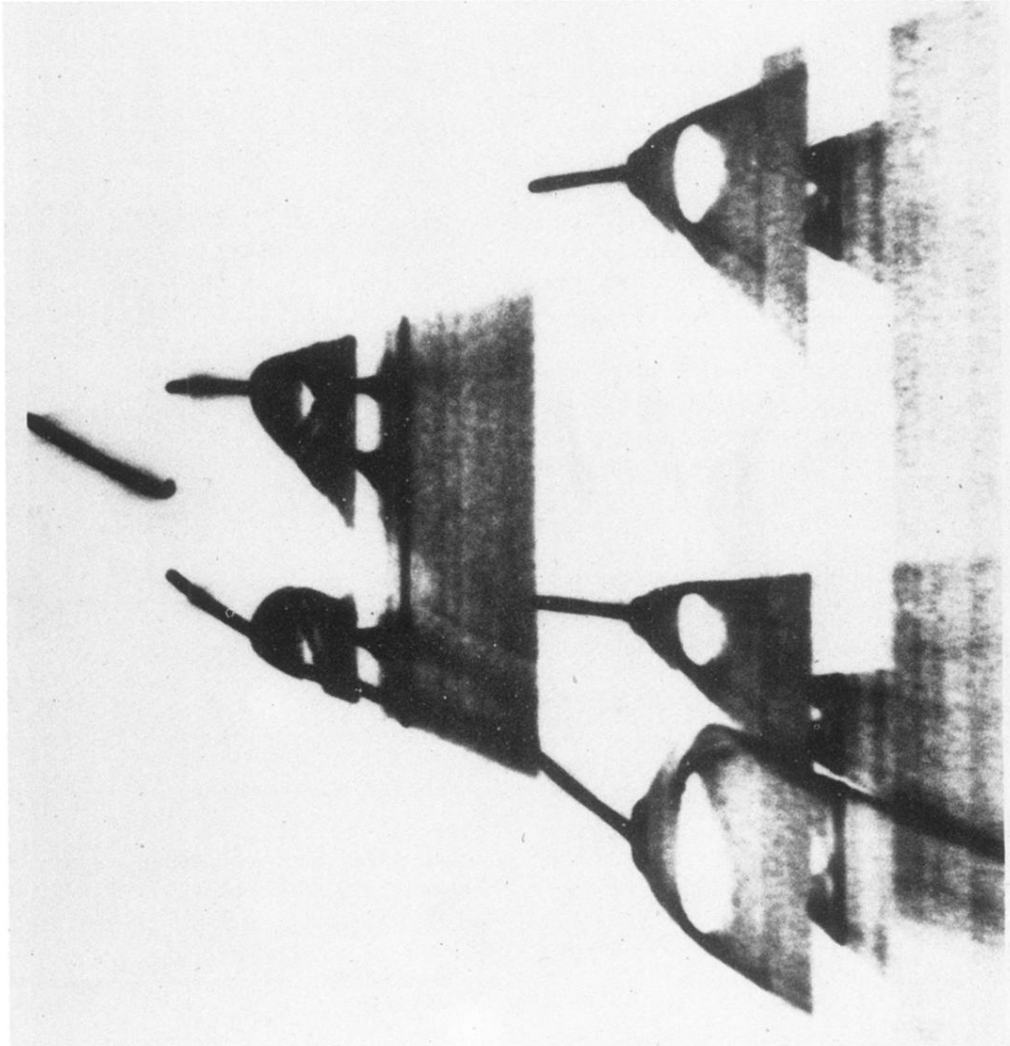


FIG. 25. Measured bifurcation diagram $[I_n]$ vs V_{os} for two identical resistively coupled junctions, $L=8.2$ mH, $R_C=100$ Ω , $f=120$ kHz, 1N4723 junction.

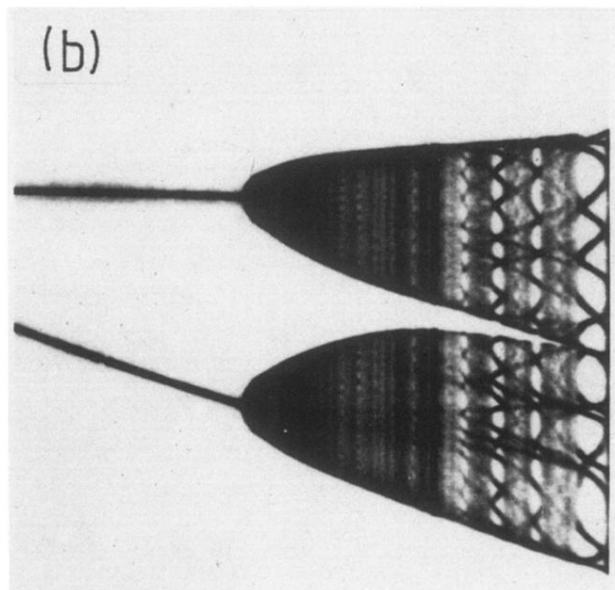
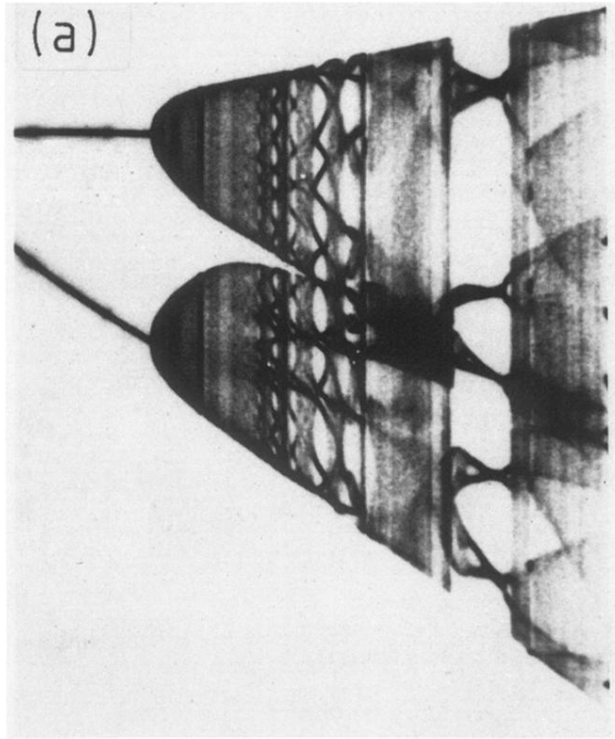


FIG. 27. (a) Observed bifurcation diagram $[I_n]$ vs V_{os} for system of Fig. 25 with coupling increased to $R_C = 1200 \Omega$. Compare to model, Fig. 28(a). (b) Expanded view of center section of (a).

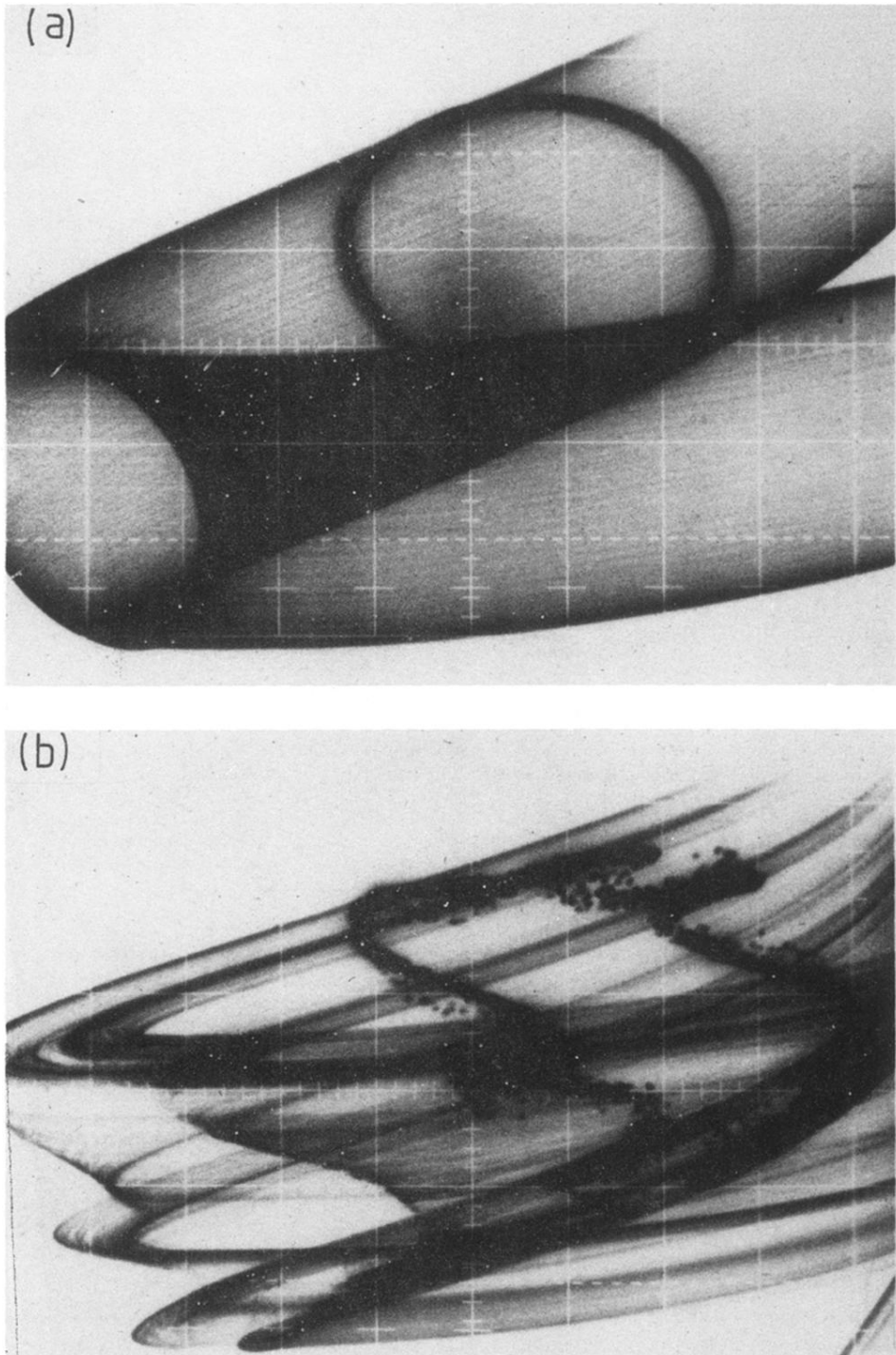


FIG. 31. (a) Phase portrait, $I_2(t)$ vs $V_1(t)$, for two resistively coupled junctions, showing piece of two-loop torus and strobed circular Poincaré section; $V_{os} = 3.2$ V rms. (b) At $V_{os} = 4.8$ V rms torus is broken up, the Poincaré section is the dark “rabbit”-like object. $L = 100$ mH, $R_C = 1200 \Omega$, $f = 27.1$ kHz, 1N4723 junction.

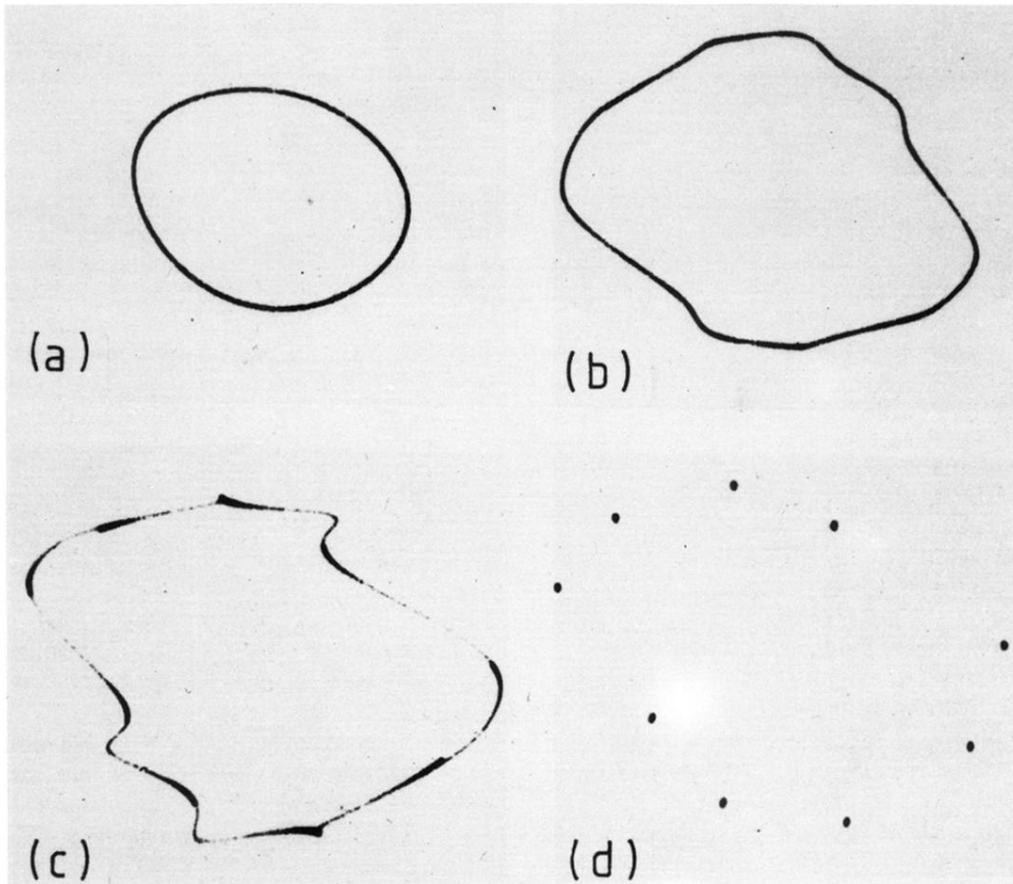


FIG. 32. Sequence of Poincaré sections, I_2 vs V_1 , for two resistively coupled junctions (Fig. 31) for increasing drive voltage V_{os} (V rms): (a) 3.165, smooth circle just after Hopf bifurcation; (b) 3.681, wrinkled circle; (c) 4.028, more wrinkled; (d) 4.190, entrainment (locking) at $f_1/f_2=18/4$.

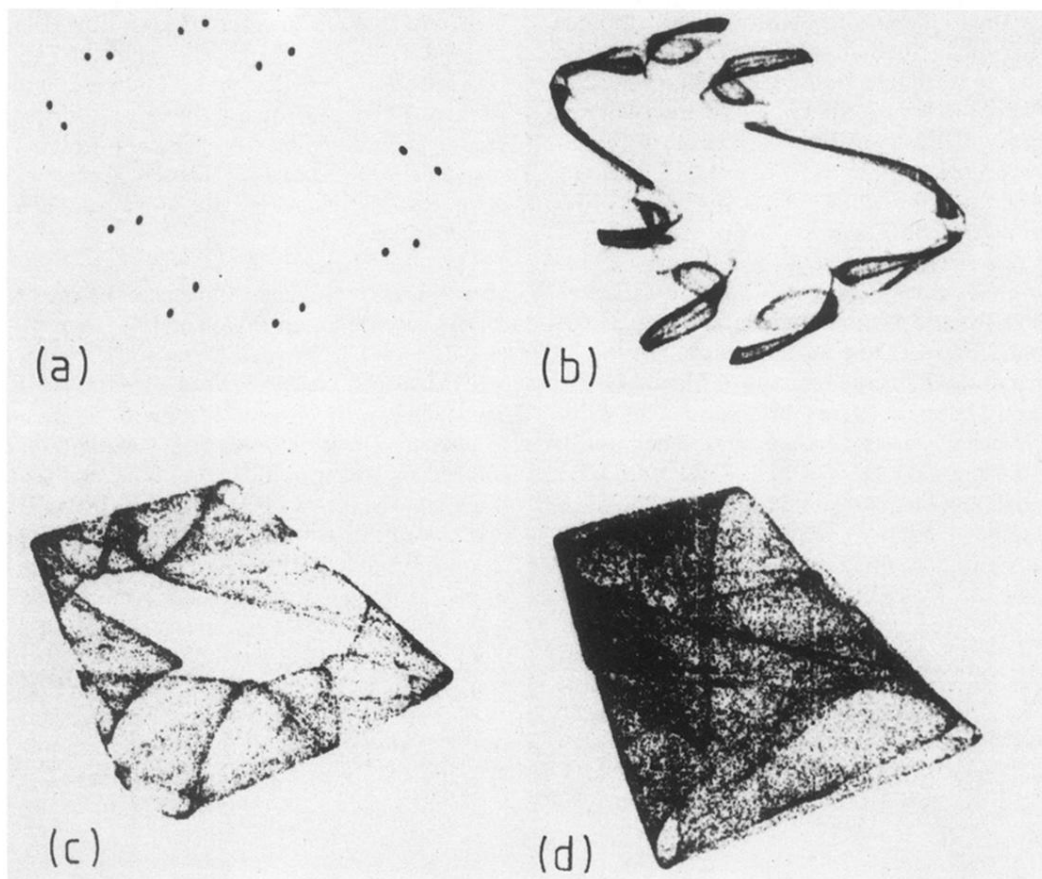


FIG. 33. Sequence of Poincaré sections, I_2 vs V_1 , continued from Fig. 32. (a) $V_{os} = 4.409$, period doubling of locked state; (b) 4.882, strange rabbit attractor; (c) 5.132, folding; (d) 8.958, more folding.

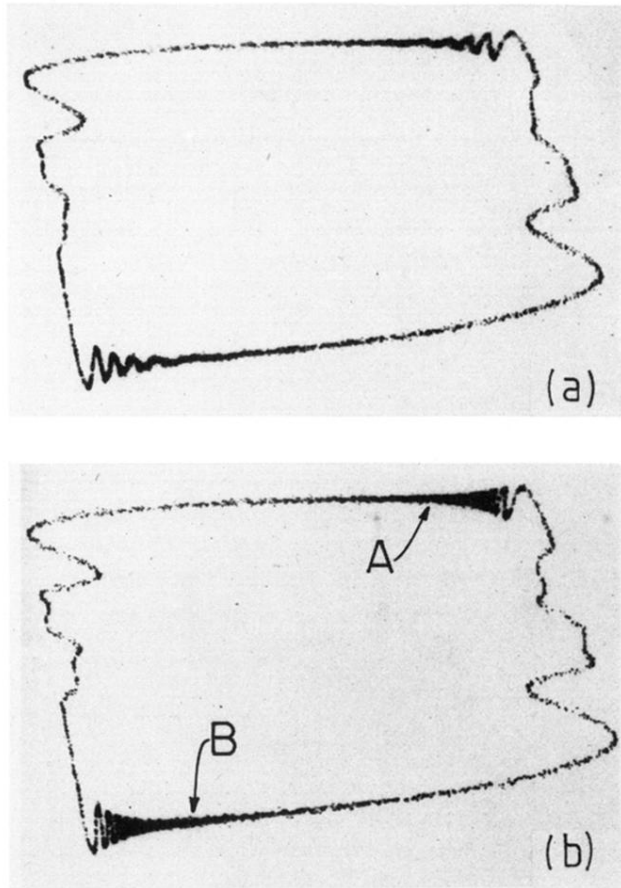


FIG. 35. Poincaré section, I_2 vs V_1 , for two resistively coupled junctions showing oscillation of the torus near period-4 locking. (a) $V_{os} = 1.976$ V rms, (b) $V_{os} = 2.003$. At $V_{os} = 2.045$ points A and B become stable fixed points. $L = 100$ mH, $R_C = 510 \Omega$, $f = 27.164$ kHz, 1N4723 junction.

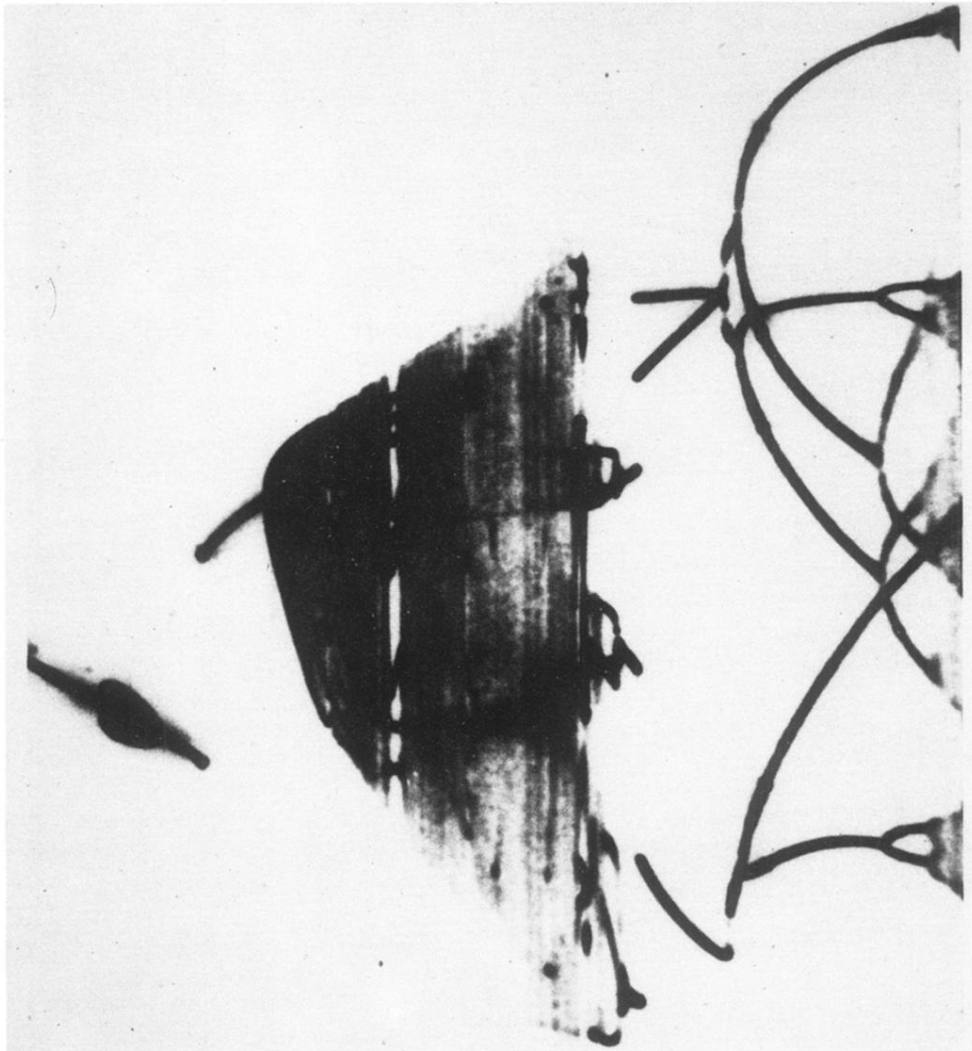


FIG. 39. Observed bifurcation diagram $[I_n]$ vs V_{os} for two identical line-coupled resonators showing Hopf bifurcation and frequency locking. $L=8.2$ mH, $R_0=70$ Ω , $f=90$ kHz, 1N4723 junction.

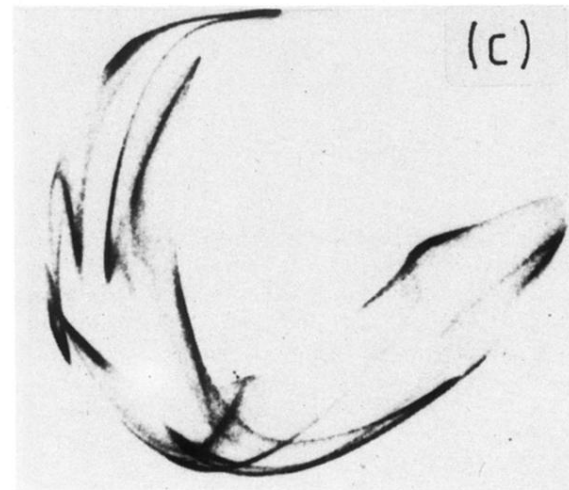
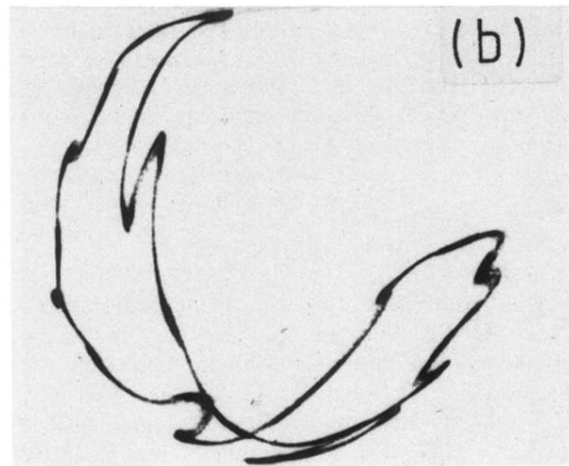
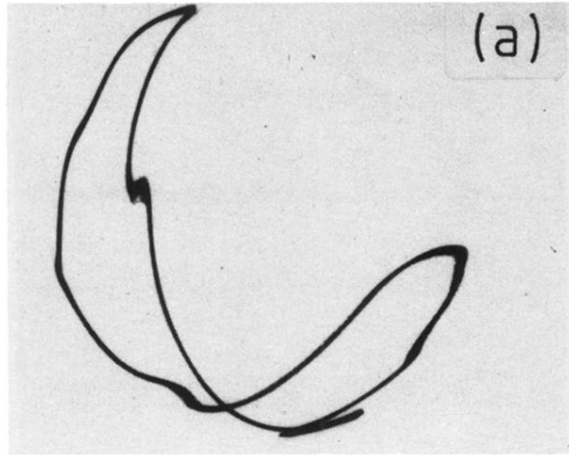


FIG. 41. Observed Poincaré sections, V_2 vs I_2 , for two line-coupled junctions for increased drive voltage, from (a) to (c), showing breakup of the torus; system same as in Fig. 39.

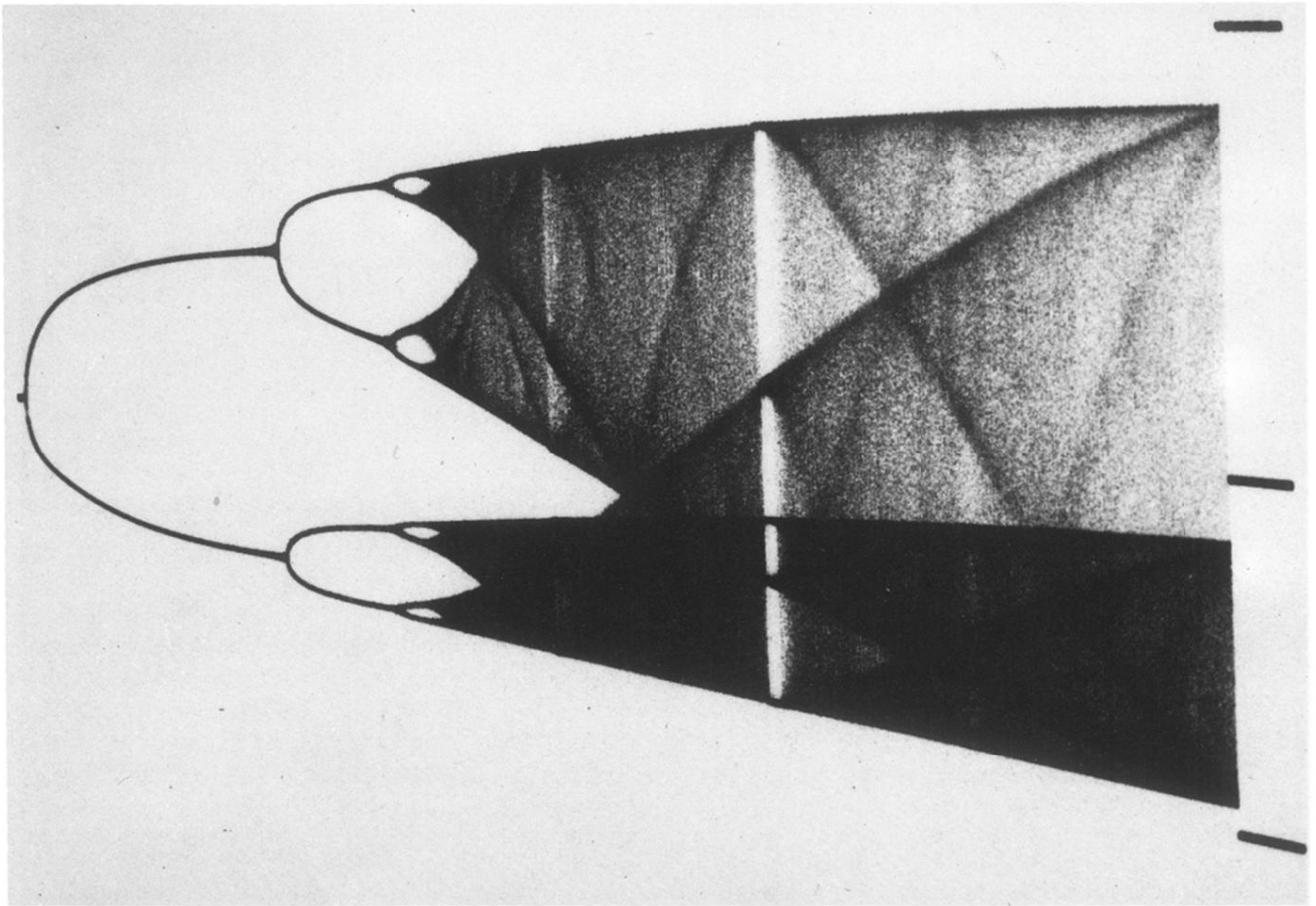


FIG. 7. Observed bifurcation diagram [I_n] vertical (arbitrary units) vs drive voltage amplitude for driven p - n junction resonator, $L=470$ mH, $f=3.87$ kHz, $R=244$ Ω , 300 A p - n junction.

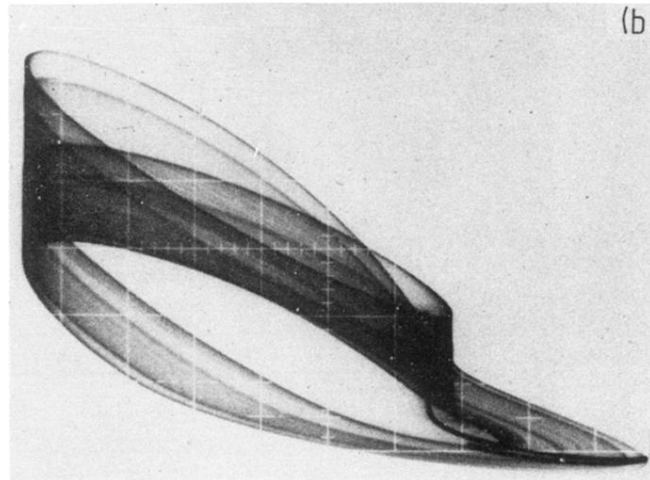
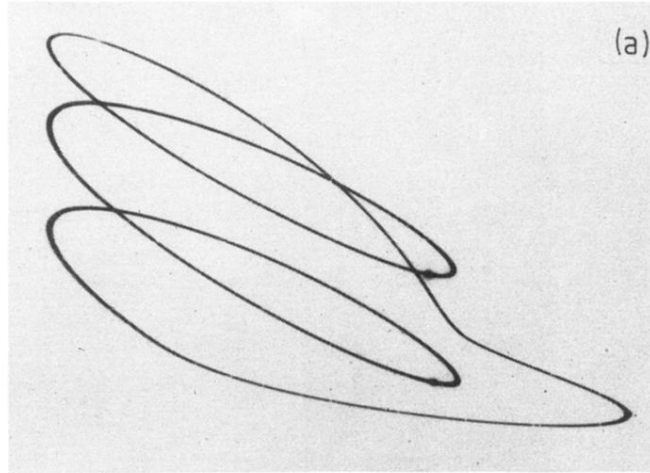


FIG. 9. (a) Observed phase portrait, I vs \dot{I} , for driven p - n junction at period-3 window: $L=100$ mH, $f=19.64$ kHz, $R=53$ Ω , 1N4723 junction, $V_{os}=3.82$ V rms; the three dark dots are a strobbed Poincaré section. (b) Phase portrait and Poincaré section (dark "bent hairpin") for same system at one-band chaos, $V_{os}=3.48$ V rms.